1   **Improving daily spatial precipitation estimates by merging gauge**

2   **observation with multiple satellite-based precipitation products**

3   **based on the geographically weighted ridge regression method**

4   Shilei Chen[a], Lihua Xiong[a,*], Qiumei Ma[b], Jong-Suk Kim[a], Jie Chen[a], Chong-Yu Xu[c]

5   [a] *State Key Laboratory of Water Resources and Hydropower Engineering Science, Wuhan*

6   *University, Wuhan, China*

7   [b] *Renewable Energy School, North China Electric Power University, Beijing, China*

8   [c] *Department of Geosciences, University of Oslo, Oslo, Norway*

9

10   *Email addresses:*

11   S. Chen (chenslwater@126.com)

12   L. Xiong (xionglh@whu.edu.cn)

13   Q. Ma (simonemaqm@163.com)

14   J-S. Kim (jongsuk@whu.edu.cn)

15   J. Chen (jiechen@whu.edu.cn)

16   C-Y. Xu (c.y.xu@geo.uio.no)

17

18   *Corresponding author:

19   Lihua Xiong, PhD, Professor

20   State Key Laboratory of Water Resources and Hydropower Engineering Science

21   Wuhan University, Wuhan, P.R. China.

22   Email: xionglh@whu.edu.cn

23   Telephone: +86-13871078660

24   Fax: +86-27-68773568

Abstract

Merging gauge observation with a single original satellite-based precipitation product (SPP) is a common approach to generate spatial precipitation estimates. For the generation of high-quality precipitation maps, however, this common method has two drawbacks: (1) the spatial resolutions of original SPPs are still too coarse; and (2) a single SPP can't capture the spatial pattern of precipitation well. To overcome these drawbacks, a two-step scheme consisting of downscaling and fusion was proposed to merge gauge observation with multiple SPPs. In both downscaling and fusion steps, the geographically weighted ridge regression (GWRR) method, which is a combination of the geographically weighted regression (GWR) method and the ridge regression method, is proposed and implemented to generate improved spatial precipitation estimates by overcoming the collinearity problem of the pure GWR method. The proposed two-step merging scheme was applied to Xijiang Basin of China deriving daily precipitation estimates from the data of both gauge observation and four near real-time SPPs (i.e., TMPA-3B42RT, CMORPH, PERSIANN and GSMaP_NRT) during the period of 2010-2017. The results showed that: (1) the collinearity problem caused by GWR was not serious in downscaling but serious enough to prevent GWR from being directly used in the fusion; and (2) the proposed two-step merging scheme significantly improved the spatial resolution and accuracy of precipitation estimates over the original SPPs. Comparisons also showed that, in the second step (fusion) of the merging scheme, the use of multiple SPPs provided more reliable spatial precipitation estimates than using a single SPP.

KEYWORDS: two-step merging scheme, multiple satellite-based precipitation products, gauge observation, geographically weighted ridge regression, collinearity problem

1. Introduction

Spatial precipitation estimates, the essential input for hydrological models, is one of the

49 atmospheric research issues most difficult to solve due to the high spatio-temporal variability

50 of precipitation (Golding 2009; Gourley and Vieux 2006; Sorooshian et al. 2011; Zhao et al.

51 2015). In the current rapid development of remote sensing techniques, satellite-based

52 precipitation product (SPP) provides an attractive source for precipitation estimates

53 characterized with extensive spatial coverage, especially for regions with complex terrain and

54 clustered in valleys where the gauge network is generally sparse (Verdin et al. 2015).

55 However, SPP inevitably contains large error because of the indirect derivation. To reduce the

56 errors of SPP, merging gauge observation that provides accurate precipitation data at point

57 locations with SPP becomes a common approach for spatial precipitation estimation

58 (AghaKouchak et al. 2009; Gebremichael et al. 2010; Yang et al. 2016; Nerini et al. 2015).

59 Great efforts have been made to develop and evaluate many different algorithms of

60 gauge-satellite precipitation merging, e.g., mean field bias correction (Huffman et al. 2007),

61 additive/multiplicative bias correction (Vila et al. 2009), statistical bias correction (Beck et al.

62 2019; Ma et al. 2019), inverse-root-mean-square-error (IRMSE) weighting (Yang et al. 2017),

63 random forest (Baez-Villanueva et al. 2020), Geographic Differential/ Ratio Analysis

64 (GDA/GRA; Cheema and Bastiaanssen 2012; Jongjin et al. 2016; Chao et al. 2018), global

65 regression models (Almazroui 2011; Cheema and Bastiaanssen 2012), Barnes objective

66 analysis (Rozante et al. 2010), Bayesian combination (BC; Nerini et al. 2015), conditional

67 merging (CM; Jongjin et al. 2016), cokriging (CK), kriging with external drift (KED; Grimes

68 et al. 1999; Manz et al. 2016), and double kernel smoothing (DS; Li and Shao 2010).

69   Most of the algorithms were developed for the merging of gauge observation and only a

70 single SPP. Although the outcomes are encouraging, it is quite a challenging job to generate

71 high-quality precipitation maps because the spatial pattern of precipitation cannot be well

72 captured by a single SPP. Derived from the signals of satellite sensors with specific retrieval

73 algorithm, the spatial pattern of precipitation in SPP is susceptible to the retrieval algorithm,

74 satellite sensors and sampling frequency, the imperfections of which will cause considerable

75 system errors in the complicated derivation process (Bharti and Singh 2015; Dinku et al.

76 2010). The marked difference in algorithm, sensors and sampling frequency for the available

77 SPPs, such as the Tropical Rainfall Measuring Mission (TRMM) Multi-satellite Precipitation

78 Analysis (TMPA; Huffman et al. 2007), Climate Prediction Center (CPC) morphing

79 technique (CMORPH; Joyce et al. 2004), Precipitation Estimation from Remotely Sensed

80 Information using Artificial Neural Networks (PERSIANN; Hsu et al. 1997 1999), Global

81 Satellite Mapping of Precipitation (GSMaP; Ushio et al. 2009), Integrated MultisatellitE

82 Retrievals for Global Precipitation Measurement (IMERG; Huffman et al. 2017), Soil

83 Moisture to Rain (SM2RAIN; Ciabatta et al. 2018) and Multi-Source Weighted-Ensemble

84 Precipitation (MSWEP; Beck et al. 2017), causes the performance of merging varies from

85 region to region, time to time, and product to product (Sun et al. 2018; Hussain et al. 2018).

86 Each product has its own strengths and weaknesses in the capture of precipitation spatial

87 pattern, and no product has been shown to be superior to others for all time and regions

88 (Maggioni et al. 2016; Sun et al. 2018). To exploit the strength of each SPP, some researchers

89 have attempted to combine multiple SPPs together and they have found that the combined

90 product provides more reliable spatial pattern estimates of precipitation compared with the

91 individual SPPs (Golian et al. 2015; Ma et al. 2017). It seems, therefore, that merging gauge

92 observation with multiple SPPs instead of a single SPP could be more conducive to the

93 improvement of spatial precipitation estimates.

94   Another restriction for estimating high-quality precipitation originates from the coarse

95 spatial resolution of SPPs released to public, which generally ranges from 0.25° to 0.05° at

96 present. Remaining the same as the SPP involved in the merging, the spatial resolution of the

97 merged precipitation product (MPP), derived from direct merging of gauge observation and

98 the original SPP performed in most previous studies, is still too coarse for local hydrological

99   and meteorological applications, as the meso- and micro-scale variability of precipitation

100   cannot be presented (Tao and Barros 2010; Xu et al. 2015). In addition, the significant

101   discrepancy in the spatial scale between coarse satellite pixels and point-based rain gauges

102   adversely affects the accuracy of the MPP (Duan and Bastiaanssen 2013). Thus, a procedure

103   spatially downscaling the original SPP will benefit to improve both the spatial resolution and

104   accuracy of the merged precipitation product. The key for spatial downscaling is to construct

105   the regression relationship between precipitation and environmental variables. By using the

106   Normalized Difference Vegetation Index (NDVI) alone as explanatory variable, Immerzeel et

107   al. (2009) successfully downscaled TRMM data on an annual scale for the first time. Taking

108   both NDVI and elevation into consideration, Jia et al. (2011) improved the downscaling

109   results of annual TRMM data. In the spatial downscaling of TRMM during six rainstorm

110   events (lasting 1-3 days per event) for the Xiao River basin, Fang et al. (2013) indicated that

111   the influence of slope, aspect and terrain roughness should not be neglected. Thereafter,

112   various environmental factors such as vegetation (e.g., NDVI), topography (e.g., elevation,

113   slope, aspect), geographical location (longitude and latitude), and land surface temperature

114   (LST) were widely used in the spatial downscaling of SPP at annual or monthly scale (Xu et

115   al. 2015; Chen et al. 2015; Jing et al. 2016; Ma et al. 2017; Zhan et al. 2018; Zhang et al.

116   2018). Due to the low correlation relationship between precipitation and environmental

117   variables at daily scale, Chen et al. (2019) and Ma et al. (2019) tried to downscale the annual

118   SPP accumulated from daily precipitation with regression model first and then disaggregate

119   the result into daily scale to generate the downscaled daily SPP.

120   To improve spatial estimates of MPP, a two-step scheme consisting of downscaling and

121   fusion for merging gauge observation with multiple SPPs is proposed in this study.

122   Geographically weighted regression (GWR, Brunsdon et al. 1996; Fotheringham et al. 2002),

123   a local form of linear regression, provides a potential method for both the spatial downscaling

124 and fusion, but probably cannot be directly used because of the collinearity problem. The

125 collinearity problem, leading to unstable and inflated parameter estimates and in extreme

126 cases even making the parameter not solvable, has been widely acknowledged as a critical

127 concern for general multivariate regression (Belsley et al. 1980; O'Brien 2007; Shieh 2011).

128 In GWR, collinearity is potentially more of a problem because of two possible reasons: (1)

129 the adverse effects can be more pronounced with smaller localized samples and (2) if the data

130 are spatially heterogeneous in terms of their correlation structure, some localities may exhibit

131 collinearity while others do not (Brunsdon et al. 2012). In both cases, GWR may be highly

132 susceptible to collinearity problem even when the problem does not exist in global datasets

133 (Wheeler and Tiefesdorf 2005). The topographic variables (e.g., elevation, slope and aspect)

134 derived from the DEM data may be related to each other, and each topographic variable may

135 also be related to the vegetation variable (e.g., NDVI). When retrieving the same precipitation

136 event, different SPPs might also have similar estimates in some areas on the condition that

137 the precipitation is well captured. Therefore, collinearity is very likely to be a problem for the

138 GWR-based downscaling-fusion scheme. One remedy for collinearity problem is to penalize

139 the size of regression coefficients with ridge regression (Hoerl and Kennard 1970; Muniz and

140 Kibria 2009). To deal with the local collinearity problems in GWR, Wheeler (2007)

141 attempted to integrate ridge regression into the GWR framework by introducing a

142 global-compensated ridge term. Then, Gollini et al. (2015) revealed that integration of ridge

143 regression and GWR is better performed using space-varying ridge parameter, thus ridge

144 regressions can only be fitted at locations in which the collinearity problem is diagnosed.

145 Despite these encouraging ideas, their tentative integration method is still inadequate for

146 practical application, as the method to remove the intercept term is not applicable to the

147 GWR frame and the criteria adopted for collinearity diagnosis gives misleading results in

148 particular cases (Lazaridis 2007; Salmeron et al. 2018). Considering these factors, the

149 geographically weighted ridge regression method (GWRR) was established by re-combining

150 ridge regression with GWR to overcome the local collinearity problem in the two-step

151 merging scheme for spatial precipitation estimation.

152   In this paper, the proposed GWRR-based two-step merging scheme was used to

153 estimate the spatial distribution of daily precipitation in the Xijiang Basin of China for the

154 period of 2010 to 2017. The rest of this paper is organized as follows. Section 2 describes the

155 study area and datasets, Section 3 presents both the proposed GWRR-based two-step merging

156 scheme and some performance evaluation indices, and Section 4-6 present the results,

157 discussion and concluding remarks, respectively.

158 2. Study Area and Datasets

159 2.1. Study Area

160   The Xijiang Basin is located in South China and has an area of 353,100 km^2, accounting

161 for 77.8% of the total area of the Pearl River Basin. As main stream of the Pearl River Basin,

162 the Xijiang River, originates from Maxiong Mountain of Yunnan Province and flows through

163 the Yunnan, Guizhou, Guangxi and Guangdong Provinces. The landform, with small and

164 scattered plains, consists mainly of mountains and hills. The basin has sub-tropical and

165 tropical monsoon climates. The mean annual temperature and precipitation are 14-22 °C and

166 1200-1900 mm, respectively. The precipitation decreases from east to west in general, and

167 numerous high and low precipitation areas are formed due to the topographic change. With

168 70%-80% of the annual precipitation occurring from April-September, precipitation is

169 unevenly distributed over a year. In this paper, the Wuzhou upstream region of Xijiang Basin

170 (Figure 1), with an area of 329,700 km^2, was selected as the study area.

171   [Figure 1 here]

172 **2.2.   Datasets**

173 **2.2.1   Rain gauge data**

174   Daily time series of 42 rain gauges (Figure 1) used in this study were provided by the

175 National Meteorological Information Center of China Meteorological Administration

176 (http://data.cma.cn). All the data were subjected to strict quality control at three levels: (1)

177 extreme values check, (2) internal consistency check, and (3) spatial consistency check (Feng

178 et al. 2004; Ma et al. 2017). The daily observation was interpreted as the 24-h accumulated

179 rainfall up to 8 p.m. Beijing time for a given day. Attributable to terrain difficulties, the rain

180 gauge network in the study area is sparse, with an average of one station for every 9,420 km^2,

181 in which situation the spatial representativeness of precipitation estimates obtained through

182 the spatial interpolation of rain gauge data is quite poor. Thus, for this study area, SPPs can

183 be attractive due to the well spatial representativeness, and the merging conducted to improve

184 the spatial precipitation estimates of SPPs seems meaningful.

185 **2.2.2   Satellite-based precipitation products (SPPs)**

186   Four level-3 near real-time SPPs, i.e., TRMM Multisatellite Precipitation Analysis 3B42

187 in Real-Time (TMPA-3B42RT), CMORPH, PERSIANN, and GSMaP in Near Real Time

188 (GSMaP_NRT), were used in the GWRR-based two-step merging scheme. The former three

189 provide 3-hourly precipitation data at 0.25° spatial resolution, and the last one provides

190 hourly precipitation at 0.1° spatial resolution. The signal inputs adopted in these products

191 come from geosynchronous infrared (IR) sensors on geostationary (GEO) satellites and

192 passive microwave (PMW) sensors on low-Earth-orbiting (LEO) satellites. IR observations

193 enable a high sampling frequency but are limited to cloud-top temperature measurements and

194 cloud height, which are not directly related to lower-level rainfall rates, while PMW imagers

195   and sounders provide more direct information about precipitation despite the poor temporal

196   sampling. The signal sources adopted in the four SPPs, especially the PMW observations,

197   exhibit large difference. In addition, different algorithms are used to retrieve spatially

198   continuous distribution information for precipitation from signal sources for the four SPPs,

199   i.e., the histogram matching method for TMPA-3B42RT, morphing technique for CMORPH,

200   adaptive artificial neural network for PERSIANN, and Kalman filter model for GSMaP_NRT.

201   The detailed information for the four products is summarized in Table 1. The daily

202   accumulations of SPPs were computed from 12 a.m. to 12 a.m. UTC to match the 8 p.m. to 8

203   p.m. Beijing time (UTC+8 time zone) of the gauge data.

204   [Table 1 here]

205   ### 2.2.3   Explanatory variables

206   The Terra Moderate Resolution Imaging Spectroradiometer (MODIS) monthly NDVI

207   products (MOD13A3) were downloaded from the NASA Land Processes Distributed Active

208   Archive Center (https://lpdaac.usgs.gov/dataset_discovery/modis) and used in this study. As

209   vegetation growth can be suppressed by water areas, urban and rural construction land, and

210   unused land, the NDVI data for these land uses no longer dominated by precipitation were

211   excluded from the original MOD13A3 and then filled with interpolated values using the

212   moving window method. Land-Use and Land-Cover Change (LUCC) with 5-year temporal

213   resolution and 1km spatial resolution, downloaded from the Resource and Environment Data

214   Cloud Platform (http://www.resdc.cn), were used to detect the excluded pixels of MOD13A3.

215   The DEM data with a 3 arc-second (~90 m) resolution was obtained from the Shuttle

216   Radar Topographic Mission (SRTM, http://srtm.csi.cgiar.org/) and resampled to 1km

217   resolution using the bilinear interpolation technique (Blue et al., 2004). Then, the variables of

218   longitude, latitude, elevation and slope data were further extracted from the resampled

219   1km-resolution DEM data with ArcGIS software.

3.   Methodology

221   A flowchart of the proposed GWRR-based two-step scheme consisting of downscaling

222   and fusion is presented in Figure 2 to illustrate the procedures of merging the gauge

223   observation with multiple SPPs. In the first step, each of four SPPs (i.e., TMPA-3B42RT,

224   CMORPH, PERSIANN and GSMaP_NRT) was downscaled to 1 km resolution separately by

225   employing the relationships between precipitation and the explanatory variables such as

226   NDVI, elevation, slope, longitude and latitude. In the second step, gauge observation was

227   fused with the four downscaled SPPs. Both the downscaling and fusion algorithm are based

228   on the geographically weighted ridge regression (GWRR) method, which was established by

229   combining ridge regression with geographically weighted regression (GWR) to overcome the

230   local collinearity problem in GWR. Collinearity refers to the strong or near to strong linear

231   correlation between the explanatory variables of linear regression model, which will lead to

232   unstable and inflated parameter estimates. In the following sections of 3.1-3.4, GWR, GWRR,

233   downscaling by GWRR, and fusion by GWRR will be introduced in detail. Section 3.5

234   presents some statistical indices for the performance evaluation of the two-step merging

235   scheme.

236   [Figure 2 here]

3.1.   Geographically weighted regression (GWR)

238   GWR is a local form of linear regression that can be used to investigate the

239   non-stationary and scale-dependent characteristics of the relationship between the dependent

240   variable and explanatory variables (Brunsdon et al. 1996; Fotheringham et al. 2002).

241   Compared with a global regression, the coefficients in GWR are functions of spatial location.

242   The GWR model can be expressed as follows:

10

243
$$y_i = \beta_{i0} + \sum_{k=1}^{p} \beta_{ik} x_{ik} + \varepsilon_i \qquad (1)$$

244 where y_i is the dependent variable at location i; x_{ik} is the kth independent variable at location i;

245 p is the number of independent variables; β_{i0} and β_{ik} $(k = 1, 2, \ldots, p)$ are the intercept and

246 slopes to be estimated at location i, respectively; and ε_i is the regression residual at location

247 i.

248   In the calibration of GWR, observations around a prediction point are weighted using a

249 distance decay function, assuming the observation closer to the location of the prediction

250 point has a greater impact on the local parameter estimates for the location. The regression

251 coefficients, including intercept β_{i0} and slopes β_{ik} $(k = 1, 2, \ldots, p)$ at location i, are

252 estimated by minimizing the weighted residual sum of squares:

253
$$\hat{\boldsymbol{\beta}}(i) = \arg\min_{\boldsymbol{\beta}} \left\{ \sum_{j=1}^{n} w_j(i) \left(y_j - \beta_{i0} - \sum_{k=1}^{p} x_{jk} \beta_{ik} \right)^2 \right\} \qquad (2)$$

254 Where $\hat{\boldsymbol{\beta}}_i = \left(\hat{\beta}_{i0}, \hat{\beta}_{i1}, \ldots, \hat{\beta}_{ip} \right)^{\mathrm{T}}$ is the vector of estimated coefficients of GWR at location

255 i, $w_j(i)$ denotes the geographical weight of j-th observation data for location i, and n is the

256 total number of observation points.

257   Equation (2) is solved by the weighted least square method, and then the regression

258 coefficients $\beta_0(u_i, v_i)$ and $\beta_k(u_i, v_i)$ can be estimated with the following matrix form:

259
$$\hat{\boldsymbol{\beta}}(i) = \left(\mathbf{X}^{\mathrm{T}} \mathbf{W}(i) \mathbf{X} \right)^{-1} \mathbf{X}^{\mathrm{T}} \mathbf{W}(i) \mathbf{y} \qquad (3)$$

260 where $\mathbf{X}$ is the matrix of independent variables with a column of 1s for the intercept,

261 $\mathbf{W}(i) = \mathrm{diag}\left[w_1(i), w_2(i), \cdots, w_n(i) \right]$ is the diagonal weights matrix denoting the

262 geographical weighting of each observed data for prediction location i, $\mathbf{y}$ is the vector of the

263 dependent variable, and superscript T indicates the matrix transpose.

264   In the GWR model, it should be emphasized, the column vectors in $\mathbf{X}$ are assumed to

265   not be linearly related to each other, which is not true in many practical applications. The

266   linear correlation between these column vectors, known as collinearity in regression, causes

267   the solution to Equation (3) to be highly problematic or even unobtainable, because in this

268   situation, the determinant of matrix $\left(\mathbf{X}^{\mathrm{T}} \mathbf{W}(i) \mathbf{X} \right)$ is close or equal to 0.

3.2.   Geographically weighted ridge regression (GWRR)

270   To overcome the collinearity problem in GWR, GWRR is established by integrating

271   ridge regression into the GWR framework. Each local GWRR model works by "shrinking"

272   the effect of the redundant variables with constrained slopes. The solution to GWRR is

273   actually a constrained minimization problem, which can be formulated as

$$\hat{\boldsymbol{\beta}}^{\mathrm{R}}(i) = \arg\min_{\boldsymbol{\beta}} \left\{ \sum_{j=1}^{n} w_j(i) \left(y_j - \beta_{i0} - \sum_{k=1}^{p} x_{jk} \beta_{ik} \right)^2 \right\}$$

$$\text{subject to} \qquad \sum_{k=1}^{p} \beta_{ik}^2 \leq \mathrm{M}(i) \tag{4}$$

275   where $\hat{\boldsymbol{\beta}}^{\mathrm{R}}(i) = \left(\hat{\boldsymbol{\beta}}_{i0}^{\mathrm{R}}, \hat{\boldsymbol{\beta}}_{i1}^{\mathrm{R}}, \cdots, \hat{\boldsymbol{\beta}}_{ip}^{\mathrm{R}} \right)^{\mathrm{T}}$ is the vector of estimated coefficients of GWRR at location i.

276   Using a Lagrange multiplier, Equation (4) can also be expressed as

$$\hat{\boldsymbol{\beta}}^{\mathrm{R}}(i) = \arg\min_{\beta} \left\{ \sum_{j=1}^{n} w_j(i) \left(y_j - \beta_{i0} - \sum_{k=1}^{p} x_{jk} \beta_{ik} \right)^2 + \lambda(i) \sum_{k=1}^{p} \beta_{ik}^2 \right\} \tag{5}$$

278   where $\lambda(i)$ is the ridge parameter that controls the amount of shrinkage in the slopes at

279   location i, and there is a one-to-one correspondence between the ridge parameter $\lambda(i)$ and

280   parameter $\mathrm{M}(i)$.

281   The intercept term β_{i0} is not constrained by the ridge parameter $\lambda(i)$ and thus should

282   be removed prior to the estimation of ridge parameter $\lambda(i)$. In addition, variables need to be

283   scaled to shake off the effects of different dimensions, as the ridge regression solution is scale

284 dependent. In the studies of Wheeler (2007) and Gollini et al. (2015), variables x and

285 y were centered to remove the intercept and standardized to eliminate the effects of different

286 dimensions. Their method stemming from general ridge regression, however, is not

287 applicable to the GWRR frame. Thus, a different method is presented as follows to obtain a

288 better ridge regression solution.

289 Based on Equation (5) above, the intercept can be estimated by Equation (6) and

290 removed through a simple transformation for local x and y variables shown in Equation (7):

291
$$\hat{\beta}_{i0}^{R} = \frac{\sum\limits_{j=1}^{n} w_j(i) y_j}{\sum\limits_{j=1}^{n} w_j(i)} - \sum\limits_{k=1}^{p} \hat{\beta}_{ik}^{R} \left(\frac{\sum\limits_{j=1}^{n} w_j(i) x_{jk}}{\sum\limits_{j=1}^{n} w_j(i)} \right) \qquad (6)$$

292
$$\ddot{x}_{jk} = x_{jk} - \frac{\sum\limits_{j=1}^{n} w_j(i) x_{jk}}{\sum\limits_{j=1}^{n} w_j(i)}, \qquad \ddot{y}_j = y_j - \frac{\sum\limits_{j=1}^{n} w_j(i) y_j}{\sum\limits_{j=1}^{n} w_j(i)} \qquad (j=1,2,\ldots,n; k=1,2,\ldots,p) \qquad (7)$$

293 where $\hat{\beta}_{i0}^{R}$ and $\hat{\beta}_{ik}^{R}(k=1,2,\cdots,p)$ are the estimated intercept and slopes of GWRR for

294 location i, respectively.

295 Then, to eliminate the effects of the different dimensions, variables $\ddot{x}$ are scaled with

296 the following equation:

297
$$x_{jk}^{*} = \frac{\ddot{x}_{jk}}{\sqrt{\sum\limits_{j=1}^{n} w_j(i)(\ddot{x}_{jk})^2}} \qquad (j=1,2,\ldots,n; \quad k=1,2,\ldots,p) \qquad (8)$$

298 The vector of scaled slopes $\hat{\boldsymbol{\beta}}^{*R}(i) = \left(\hat{\beta}_{i1}^{*R}, \hat{\beta}_{i2}^{*R}, \ldots, \hat{\beta}_{ip}^{*R} \right)^{T}$ in GWRR model is obtained as

299
$$\hat{\boldsymbol{\beta}}^{*R}(i) = \left(\mathbf{X}_w^{*T} \mathbf{X}_w^{*} + \lambda(i) \mathbf{I}_p \right)^{-1} \mathbf{X}_w^{*T} \ddot{\mathbf{y}}_w \qquad (9)$$

300 where $\mathbf{X}_w^{*}$ is the matrix of weighted x^{*} variables $\sqrt{w} x^{*}$, $\ddot{\mathbf{y}}_w$ is the vector of

301 weighted $\ddot{y}$ variable $\sqrt{w} \ddot{y}$, and $\mathbf{I}_p$ is the $(p \times p)$ identity matrix.

302   The original slopes used for estimating the dependent variable are

$$\hat{\beta}_{ik}^{R} = \hat{\beta}_{ik}^{*R} \times \sqrt{\sum_{j=1}^{n} w_j(i)(\ddot{x}_{jk})^2} \quad (k=1,2,...,p) \qquad (10)$$

304   With the estimated intercept $\hat{\beta}_{i0}^{R}$ and slopes $\hat{\beta}_{ik}^{R}(k=1,2,\cdots,p)$, the dependent variable

305   at location i can be estimated as

$$\hat{y}_i^{R} = \hat{\beta}_{i0}^{R} + \sum_{k=1}^{p} \hat{\beta}_{ik}^{R} x_{ik} \quad (k=1,2,...,p) \qquad (11)$$

307   Note that if the ridge parameter $\lambda(i)$ is 0, the GWRR estimator coincides with the

308   GWR estimator. In our integration framework, ridge regression was only fitted at locations

309   where collinearity was strong enough to be a problem. To achieve this goal, the local ridge

310   parameter was initially set as 0 and re-estimated when collinearity problem was diagnosed.

311   Condition number (CN), a very stable procedure in comparison to other tests, was preferred

312   as the diagnosis indicator of collinearity problem in this study. For a column-scaled matrix $\mathbf{X}$

313   (each column has unit length), the CN is defined as

$$CN(\mathbf{X}) = \frac{\mu_{max}}{\mu_{min}} \qquad (12)$$

315   where μ_{max} and μ_{min} are the maximum and minimum singular values of matrix $\mathbf{X}$,

316   respectively, which can be obtained by applying singular value decomposition (SVD) to

317   matrix $\mathbf{X}$.

318   The larger the CN value, the stronger is the collinearity among the columns of matrix $\mathbf{X}$.

319   Collinearity has almost no effect on estimation results with a low CN value and is strong

320   enough to be a problem when the CN of the design matrix exceeds a certain threshold level.

321   In extreme cases where the CN of the design matrix tends to be infinite, perfect collinearity,

322   which makes the regression equation unsolvable, is produced. The threshold CN of 30 for the

323   intercept-included and column-scaled design matrix, used in most previous collinearity

324   diagnosis, has already proved to give misleading results in particular cases and should be

325   replaced by the threshold CN of 5.42 for the intercept-excluded and column-scaled design

326   matrix $\mathbf{X}^*$ to achieve a better diagnosis (Lazaridis. 2007; Salmeron et al. 2018).

327   To test the presence of the collinearity problem after the constraint of slopes, the CN in

328   ridge regression must also be estimated. Unlike the CN in general linear regression, the CN in

329   ridge regression cannot be directly estimated because the design matrix $\mathbf{X}^R = \begin{pmatrix} \mathbf{X}^* \\ \sqrt{\lambda}\mathbf{I}_p \end{pmatrix}$ does

330   not have vectors of unit length. To extend the diagnosis to ridge regression, Salmeron et al

331   (2018) compared two extensions of the CN in ridge regression: one accessible but unnatural

332   (given the definition of CN) and one natural but inaccessible, and they found that the two

333   extensions led to very similar results. Being able to present an algebraic closed-form

334   expression for the CN in ridge regression, the unnatural extension is easier to apply and can

335   be used to determine the ridge parameter. Suppose the intercept-excluded and column-scaled

336   design matrix $\mathbf{X}^*$ has singular values of $\mu_1, \mu_2, \cdots, \mu_p (\mu_1 < \mu_2 < \cdots < \mu_p)$, then the singular

337   values of matrix $\mathbf{X}^R = \begin{pmatrix} \mathbf{X}^* \\ \sqrt{\lambda}\mathbf{I}_p \end{pmatrix}$ are $\sqrt{\mu_1^2 + \lambda}, \sqrt{\mu_2^2 + \lambda}, \cdots, \sqrt{\mu_p^2 + \lambda}$, and thus the close-form

338   expression of the CN in ridge regression can be given by $\mathrm{CN}(\mathbf{X}^R) = \sqrt{\dfrac{\mu_p^2 + \lambda}{\mu_1^2 + \lambda}}$. By setting

339     $\mathrm{CN}(\mathbf{X}^R)$ as the threshold of 5.42 to protect the ridge regression from collinearity problem,

340   the ridge parameter can be determined as:

341
$$\lambda = \frac{\mu_p^2 - 5.42^2 \cdot \mu_1^2}{5.42^2 - 1} \tag{13}$$

342   Taking matrix $\mathbf{X}_w^*$ mentioned above instead of matrix $\mathbf{X}^*$ as the design matrix, the

343   method for collinearity diagnosis and elimination can be migrated from general linear

344   regression to GWR.

345   Solving the GWR or GWRR equations first requires an estimation of the spatial weights

346   matrix $\mathbf{W}(i) = \mathrm{diag}\left[w_1(i), w_2(i), \cdots, w_n(i) \right]$. A kernel that is commonly used to calculate

347   the weights matrix is the bi-square function, where the weight of observation at location j for

348   estimating the dependent variable at location i is given by

$$w_j(i) = \begin{cases} [1 - (d_{ij}/b)^2]^2 & d_{ij} \leq b \\ 0 & d_{ij} > b \end{cases} \tag{14}$$

350   where d_{ij} is the Euclidean distance between prediction location i and observation location j;

351   and b is the kernel bandwidth. An optimum bandwidth can be found by minimizing the

352   cross-validation (CV) score (Bowman. 1984), given as:

$$CV = \sum_{j=1}^{n} \left[y_j - \hat{y}_{\neq j}(b) \right]^2 \tag{15}$$

354   where $\hat{y}_{\neq j}(b)$ is the estimated value of y_j with the observation for location j omitted from

355   the calibration process.

3.3.   Downscaling by GWRR

357   The downscaling algorithm is based on the assumption that the GWRR relationship

358   between precipitation and explanatory variables (i.e., NDVI, elevation, slope, longitude and

359   latitude) constructed at original coarse resolution can be used to predict precipitation with the

360   explanatory variables at a finer resolution. The residuals of GWRR model were considered to

361   have some spatial correlation (Kumar et al. 2012, Harris et al. 2010; Ye et al. 2017) and thus

362   were interpolated using ordinary Kriging to improve the prediction accuracy. Since the

363   relationship between precipitation and environmental variables at daily scale is far less

364   statistically significant than that at annual and monthly scale (Chen et al. 2019; Ma et al

365   2019), we constructed the GWRR model at monthly scale and then disaggregated the

366 downscaled monthly result into daily precipitation to generate the downscaled daily SPP. It is

367 noted that precipitation and NDVI of the same period were used to construct the GWRR

368 model for downscaling monthly SPP, as vegetation conditions can disturb the spatial

369 distribution of precipitation nearly without time lag (Brunsell 2006; Xu et al. 2015). The

370 specific steps of the downscaling algorithm based on GWRR are as follows:

371   (1) Resample the original NDVI, elevation, slope, longitude and latitude data of 1km

372 resolution to 0.25° and 0.1° resolutions respectively by pixel averaging. The original

373 1km-resolution NDVI of month m, and the elevation, slope, longitude and latitude for

374 location i are denoted by $NDVI_{i,m}^{1km}$, $Elevation_i^{1km}$, $Slope_i^{1km}$, $Longitude_i^{1km}$, and $Latitude_i^{1km}$,

375 respectively; and the corresponding resampled results with 0.25° resolution and 0.1°

376 resolution are denoted as $NDVI_{i,m}^{0.25^o}$, $Elevation_i^{0.25^o}$, $Slope_i^{0.25^o}$, $Longitude_i^{0.25^o}$,

377 $Latitude_i^{0.25^o}$, and $NDVI_{i,m}^{0.1^o}$, $Elevation_i^{0.1^o}$, $Slope_i^{0.1^o}$, $Longitude_i^{0.1^o}$, $Latitude_i^{0.1^o}$,

378 respectively.

379   (2) Accumulate original satellite daily precipitation to generate monthly precipitation,

380 and construct the GWRR model for downscaling the satellite monthly precipitation with the

381 resampled NDVI, elevation, slope, longitude and latitude generated by step (1) as

382 independent variables. The original 0.25° and 0.1°-resolution satellite daily precipitation for

383 location i and day d are denoted by $P_{i,d}^{0.25^o,\,SAT}$ ($P_{i,d}^{0.25^o,TMP}$ for TMPA-3B42RT, $P_{i,d}^{0.25^o,\,CMO}$ for

384 CMORPH and $P_{i,d}^{0.25^o,PER}$ for PERSIANN) and $P_{i,d}^{0.1^o,\,SAT}$ (i.e. $P_{i,d}^{0.1^o,GSM}$ for GSMaP_NRT),

385 respectively; and the corresponding accumulated satellite monthly precipitation for location i

386 and month m are denoted by $P_{i,m}^{0.25^o,SAT}$ ($P_{i,m}^{0.25^o,TMP}$ for TMPA-3B42RT, $P_{i,m}^{0.25^o,\,CMO}$ for

387 CMORPH, and $P_{i,m}^{0.25^o,PER}$ for PERSIANN) and $P_{i,m}^{0.1^o,SAT}$ (i.e. $P_{i,m}^{0.1^o,GSM}$ for GSMaP_NRT),

388 respectively.

389   For the 0.25°-resolution satellite monthly precipitation $P_{i,m}^{0.25°,\text{SAT}}$, the constructed

390   GWRR model for downscaling is expressed as:

391
$$P_{i,m}^{0.25°,\text{SAT}} = \alpha_{i,m}^{\text{SAT},0} + \alpha_{i,m}^{\text{SAT},1} NDVI_{i,m}^{0.25°} + \alpha_{i,m}^{\text{SAT},2} Elevation_i^{0.25°} + \alpha_{i,m}^{\text{SAT},3} Slope_i^{0.25°} + \alpha_{i,m}^{\text{SAT},4} Longitude_i^{0.25°}$$
$$+\alpha_{i,m}^{\text{SAT},5} Latitude_i^{0.25°} + \varepsilon_{i,m}^{0.25°,\text{SAT}} \tag{16a}$$

392   And for the 0.1°-resolution satellite monthly precipitation $P_{i,m}^{0.1°,\text{SAT}}$, the constructed

393   GWRR model for downscaling is expressed as:

394
$$P_{i,m}^{0.1°,\text{SAT}} = \alpha_{i,m}^{\text{SAT},0} + \alpha_{i,m}^{\text{SAT},1} NDVI_{i,m}^{0.1°} + \alpha_{i,m}^{\text{SAT},2} Elevation_i^{0.1°} + \alpha_{i,m}^{\text{SAT},3} Slope_i^{0.1°} + \alpha_{i,m}^{\text{SAT},4} Longitude_i^{0.1°}$$
$$+\alpha_{i,m}^{\text{SAT},5} Latitude_i^{0.1°} + \varepsilon_{i,m}^{0.1°,\text{SAT}} \tag{16b}$$

395   where $\alpha_{i,m}^{\text{SAT},0}$, $\alpha_{i,m}^{\text{SAT},1}$, $\alpha_{i,m}^{\text{SAT},2}$, $\alpha_{i,m}^{\text{SAT},3}$, $\alpha_{i,m}^{\text{SAT},4}$ and $\alpha_{i,m}^{\text{SAT},5}$ are regression coefficients for

396   location i and month m ($m = 1,2,\ldots,96$ for the period of 2010 to 2017), and

397    $\varepsilon_{i,m}^{0.25°,\text{SAT}}$ and $\varepsilon_{i,m}^{0.1°,\text{SAT}}$ are the residual with 0.25° resolution and 0.1° resolution for location i

398   and month m, respectively, which can be interpreted as the amount of satellite precipitation

399   that is not be explained by the constructed GWRR model for downscaling. The regression

400   coefficients and residual are estimated in this step.

401   (3) Resample the regression coefficients $\alpha_{i,m}^{\text{SAT},0}$, $\alpha_{i,m}^{\text{SAT},1}$, $\alpha_{i,m}^{\text{SAT},2}$, $\alpha_{i,m}^{\text{SAT},3}$, $\alpha_{i,m}^{\text{SAT},4}$ and

402    $\alpha_{i,m}^{\text{SAT},5}$ obtained by step (2) to acquire the 1km-resolution regression coefficients $\alpha_{i,m}^{1\text{km},\text{SAT},0}$,

403    $\alpha_{i,m}^{1\text{km},\text{SAT},1}$, $\alpha_{i,m}^{1\text{km},\text{SAT},2}$, $\alpha_{i,m}^{1\text{km},\text{SAT},3}$, $\alpha_{i,m}^{1\text{km},\text{SAT},4}$ and $\alpha_{i,m}^{1\text{km},\text{SAT},5}$ with the bilinear interpolation

404   technique.

405   (4) Estimate the 1km-resolution satellite monthly precipitation $\hat{P}_{i,m}^{1\text{km},\text{SAT}}$

406   from $NDVI_{i,m}^{1\text{km}}$, $Elevation_i^{1\text{km}}$, $Slope_i^{1\text{km}}$, $Longitude_i^{1\text{km}}$, and $Latitude_i^{1\text{km}}$ using the

407   resampled 1km-resolution regression coefficients:

408
$$\hat{P}_{i,m}^{1\text{km},\text{SAT}} = \alpha_{i,m}^{1\text{km},\text{SAT},0} + \alpha_{i,m}^{1\text{km},\text{SAT},1} NDVI_{i,m}^{1\text{km}} + \alpha_{i,m}^{1\text{km},\text{SAT},2} Elevation_i^{1\text{km}} + \alpha_{i,m}^{1\text{km},\text{SAT},3} Slope_i^{1\text{km}}$$
$$+\alpha_{i,m}^{1\text{km},\text{SAT},4} Longitude_i^{1\text{km}} + \alpha_{i,m}^{1\text{km},\text{SAT},5} Latitude_i^{1\text{km}} \tag{17}$$

409 As the resampling process in step (1) smooths the extreme values, the obtained regression

410 coefficients and $\hat{P}_{i,m}^{1km,SAT}$ over the high-resolution grid-cells with extreme NDVI or elevation

411 values may have poor performance.

412   (5) Interpolate the 0.25° or 0.1°-resolution residuals $\varepsilon_{i,m}^{0.25°,SAT}$ or $\varepsilon_{i,m}^{0.1°,SAT}$ to obtain the

413 1km-resolution residuals $\varepsilon_{i,m}^{1km,SAT}$ using ordinary kriging method, and then add the

414 interpolated residuals $\varepsilon_{i,m}^{1km,SAT}$ to the estimated satellite monthly precipitation $\hat{P}_{i,m}^{1km,SAT}$ by

415 equation (17) to generate the GWRR-downscaled satellite monthly precipitation $P_{i,m}^{1km,SAT}$,

416 which is denoted as $P_{i,m}^{1km,TMP}$ for TMPA-3B42RT, as $P_{i,m}^{1km,CMO}$ for CMORPH, as $P_{i,m}^{1km,PER}$ for

417 PERSIANN, and as $P_{i,m}^{1km,GSM}$ for GSMaP_NRT, namely:

418
$$P_{i,m}^{1km,SAT} = \hat{P}_{i,m}^{1km,SAT} + \varepsilon_{i,m}^{1km,SAT} \tag{18}$$

419   (6) Disaggregate the downscaled satellite monthly precipitation into daily precipitation.

420 Assuming that the occurrence of rainfall events is correctly detected, the fraction of each

421 daily precipitation to the monthly total precipitation at original 0.25° or 0.1° resolution,

422 denoted by $F_{i,d}^{0.25°,SAT}$ or $F_{i,d}^{0.1°,SAT}$, can be obtained from the original SPP data ($P_{i,d}^{0.25°,SAT}$ or

423 $P_{i,d}^{0.1°,SAT}$). The $F_{i,d}^{0.25°,SAT}$, for example, is expressed with the following equation:

424
$$F_{i,d}^{0.25°,SAT} = \frac{P_{i,d}^{0.25°,SAT}}{P_{i,m}^{0.25°,SAT}} \tag{19}$$

425 Then, $F_{i,d}^{0.25°,SAT}$ or $F_{i,d}^{0.1°,SAT}$ was further resampled to 1km resolution with the bilinear

426 interpolation technique, denoted by $F_{i,d}^{1km,SAT}$.

427   (7) The downscaled satellite daily precipitation $P_{i,d}^{1km,SAT}$, which is denoted as

428 $P_{i,d}^{1km,TMP}$ for TMPA-3B42RT, $P_{i,d}^{1km,CMO}$ for CMORPH, $P_{i,d}^{1km,PER}$ for PERSIANN, $P_{i,d}^{1km,GSM}$ for

429 GSMaP_NRT, can be acquired by multiplying the 1km-resolution daily fractions by the

430   downscaled satellite monthly precipitation:

431
$$P_{i,d}^{\text{1km, SAT}} = F_{i,d}^{\text{1km, SAT}} \cdot P_{i,m}^{\text{1km, SAT}} \tag{20}$$

3.4.   Fusion by GWRR

433   Regarding gauge precipitation as the actual and neglecting the influence of scaling gaps

434   between gauge precipitation and satellite precipitation, the fusion can be performed with the

435   functional relationship between gauge precipitation and multiple satellites precipitation

436   constructed with the GWRR method. Given that the model validity will be undermined by the

437   spatially intermittency of daily precipitation, the Box-Cox transformed precipitation data are

438   used in the GWRR model construction. The constructed GWRR model for fusion can be

439   expressed with the following equation:

440
$$\frac{\left(P_{i,d}^{Gauge}\right)^{\delta}-1}{\delta} = \beta_{i,d}^{0} + \beta_{i,d}^{1}\frac{\left(P_{i,d}^{\text{1km,TMP}}\right)^{\delta}-1}{\delta} + \beta_{i,d}^{2}\frac{\left(P_{i,d}^{\text{1km,CMO}}\right)^{\delta}-1}{\delta} + \beta_{i,d}^{3}\frac{\left(P_{i,d}^{\text{1km,PER}}\right)^{\delta}-1}{\delta}$$
$$+ \beta_{i,d}^{4}\frac{\left(P_{i,d}^{\text{1km,GSM}}\right)^{\delta}-1}{\delta} + \varepsilon_{i,d} \tag{21}$$

441   where $P_{i,d}^{Gauge}$ is the gauge precipitation at location i for day d; $\beta_{i,d}^{0}$, $\beta_{i,d}^{1}$, $\beta_{i,d}^{2}$, $\beta_{i,d}^{3}$

442   and $\beta_{i,d}^{4}$ are regression coefficients at location i for day d; $\varepsilon_{i,d}$ is the residual at

443   location i for day d; δ is the parameter in Box-Cox transformation. As indicated by

444   Erdin et al. (2012), the optimal δ value varies slightly with the days, with 87% ranging from

445   0.2 to 0.3 and a mean close to 0.25 over one year. This explains why the results of a fixed

446   δ value of 0.25 (Cecinati et al., 2017; Gurung 2017) or 0.2 (Delrieu et al., 2014) are

447   satisfactory and very similar with that of the optimal and time-variant δ value. In this paper,

448   a fixed value of 0.25 is set for δ.

449   The fusion regression coefficients in equation (21) at any 1km grid cell can be obtained

450   from gauge observation and the four downscaled SPPs, i.e., $P_{i,d}^{\text{1km,TMP}}$, $P_{i,d}^{\text{1km,CMO}}$, $P_{i,d}^{\text{1km,PER}}$

451 and $P_{i,d}^{1km,GSM}$, with which the daily precipitation at any 1km grid cell, denoted by

452 $\hat{P}_{i,d}^{1km,GWRR}$ for location i and day d, can be estimated by the following equation:

453
$$\frac{\left(\hat{P}_{i,d}^{1km,GWRR}\right)^{\delta}-1}{\delta}=\beta_{i,d}^{0}+\beta_{i,d}^{1}\frac{\left(P_{i,d}^{1km,TMP}\right)^{\delta}-1}{\delta}+\beta_{i,d}^{2}\frac{\left(P_{i,d}^{1km,CMO}\right)^{\delta}-1}{\delta}+\beta_{i,d}^{3}\frac{\left(P_{i,d}^{1km,PER}\right)^{\delta}-1}{\delta}$$
$$+\beta_{i,d}^{4}\frac{\left(P_{i,d}^{1km,GSM}\right)^{\delta}-1}{\delta} \tag{22}$$

454 The residuals obtained only at gauge sites from equation (21) are interpolated to obtain

455 the residuals for all 1km grid cells, denoted by $\varepsilon_{i,d}^{1km}$ for location i and day d, using

456 ordinary Kriging method. Finally, the daily estimates of the merged precipitation product

457 (MPP) for 1km resolution by the two-step scheme (downscaling and fusion) using the GWRR

458 method , which is denoted by $P_{i,d}^{1km,MPP}$, can be calculated as:

459
$$P_{i,d}^{1km,MPP}=\hat{P}_{i,d}^{1km,GWRR}+\varepsilon_{i,d}^{1km} \tag{23}$$

3.5.   Performance evaluation indices

461 A set of statistical indices, including continuous indices and categorical indices, were

462 examined to evaluate the leave-one-out cross validation results of the GWRR-based two-step

463 merging scheme. The statistical metrics used in this study are listed in Table 2.

464 [Table 2 here]

3.5.1   Continuous indices

466 The correlation coefficient (CC) reflects the degree of linear correlation between the

467 estimations and observations; the mean error (ME) simply scales the general deviation of

468 estimations from the observations, the relative bias (rBIAS) describes the systematic bias of

469 estimations, and the modified Kling-Gupta efficiency (KGE; Kling et al., 2012) incorporates

470 three components, i.e., the correlation coefficient, the bias ratio, and the variability ratio to

471 compare observations with estimations. Moreover, centered root-mean square difference

472 (RMSD) was also calculated for the Taylor diagram (Taylor 2001), which is drawn to visually

473 show how closely the retrieved precipitation match the gauge observation and can be

474 beneficial for evaluating the relative accuracy of various SPPs.

3.5.2 Categorical indices

476 To quantitatively evaluate the precipitation detection ability of SPP against the gauge

477 observation over different precipitation intensities, four categorical statistical indices,

478 including probability of detection (POD), false alarm ratio (FAR), the frequency bias index

479 (FBI) and critical success index (CSI) were also calculated. POD, also known as the hit rate,

480 describes how often the SPP correctly detects the precipitation event. FAR measures the

481 proportion of cases in which the satellite identify the event when rain gauges do not. FBI

482 compares the number of events identified by the SPP to the number of events registered by

483 the gauge station. If FBI > 1, the number of occurrences of the respective precipitation event

484 is overestimated by the SPP, while FBI < 1 indicates underestimation. CSI shows the overall

485 ability of SPP to correctly diagnose different precipitation events.

4. Results

4.1. The collinearity problem in the GWR-based merging scheme

488 The collinearity problem, which appears when CN reaches the threshold CN value of

489 5.42, leads to unstable and inflated parameter estimates. The collinearity problem in extreme

490 cases where CN tends to be infinite, which is termed as perfect collinearity problem, even

491 makes the parameter of GWR unsolvable. To quantity the overall occurrence of these two

492 problems, collinearity rate (CR) and perfect collinearity rate (PCR) were defined as the ratio

493 of the number of times the collinearity problem and perfect collinearity problem occurred to

494 the total number of times the GWR model was fitted during a certain period, respectively.

495   Figure 3 presents the spatial distribution of CR in the GWR model for downscaling

496   monthly SPP (without integration of ridge regression) from 2010-2017. It can be seen that

497   GWR models for downscaling 0.25°-resolution TMPA-3B42RT, CMORPH and PERSIANN

498   were more likely to suffer from collinearity problem than those for downscaling

499   0.1°-resolution GSMaP_NRT. Furthermore, the GWR models for downscaling developed at

500   the same resolution had similar collinearity problem, with CR values less than 30% in

501   depression areas and greater than 70% in many other areas. The small difference in CR of

502   GWR model for downscaling TMPA-3B42RT, CMORPH and PERSIANN could be

503   attributed to the different optimal bandwidth selected to fit the GWR model, which depended

504   on the data quality of SPP. The PCR of GWR model for downscaling was zero for all the

505   regions, indicating that the perfect collinearity problem will never trouble the GWR model

506   for downscaling. In addition, apart from adopting GWRR method, the collinearity problem

507   existed in the GWR model for downscaling can be alternatively addressed by enlarging the

508   sample size, since there are so many samples (satellite precipitation pixels) can be used. With

509   respect to the GWR model for fusion (without integration of ridge regression), the PCR

510   ranged from 30% to 48% at 42 gauge locations, which was approximately 20% less than CR

511   (Figure 5). Such a high PCR value indicated that it was urgent to overcome the collinearity

512   problem in the GWR model for fusion to achieve stable parameter estimates. High values of

513   CR and PCR in the GWR model for fusion also occurred in regions close to the border where

514   few samples were used for model fitting. Excluding the effect of sample size, CR and PCR of

515   the GWR model for fusion in the eastern plains had higher values than in the middle hills and

516   western mountains. Limited by few gauge observations, the collinearity problem in the GWR

517   model for fusion cannot be addressed by simply enlarging the sample size, which is different

518   from the GWR model for downscaling.

519   [Figure 3 here]

520 <center>[Figure 4 here]</center>

4.2. Assessment of the GWRR-based merging scheme

4.2.1 Local regression analysis

523   The GWRR model for fusion exploits the strength and minimizes the weakness of each
524 SPP member with time-varying and space-varying regression coefficients, which are
525 determined by the performance of SPPs. The well performing SPP member will receive a
526 positive and large coefficient, the ordinarily performing SPP member will receive a negative
527 coefficient, and the poorly performing SPP member will receive a coefficient close to 0. In
528 particular cases presenting collinearity problem, some SPP members will also receive a
529 coefficient that is arbitrarily close to zero, regardless of the performance. The GWRR-based
530 proceeding dealing with perfect collinearity problem can be regarded as a process of variable
531 selection, in which the redundant SPP members are removed from the regression.

532   Figure 5 displays the spatial pattern of the regression coefficients of the GWRR model
533 for fusion on two typical days: June 21 and September 30, 2014. All the regression
534 coefficients for the Box-Cox transformed downscaled SPP had numerous values that were far
535 away from 0, indicating that none of the four SPPs was useless and that using multiple SPPs
536 seemed to benefit the fusion result. In addition, all the regression coefficients unevenly
537 distributed in space were markedly different between the two days. In terms of the area
538 average of the regression coefficients for Box-Cox transformed downscaled SPPs, the order
539 was β^4 (1.04) $> \beta^2$ (0.30) $> \beta^1$ (-0.03)$> \beta^3$ (-0.31) on June 21, 2014, and was
540 β^4 (1.21) $> \beta^2$ (0.39) $> \beta^3$ (0.08) $> \beta^1$ (-0.18) on September 30, 2014. The area average of β^0
541 was 0.73 mm on June 21, 2014 and was 0.93mm on September 30, 2014. As for the spatial
542 pattern of the regression coefficients, the differences between the two days were manifested
543 in the northern region for β^1, β^3 and β^4, as well as in the central region for β^2. This

<center>24</center>

544 result suggested the presence of spatiotemporal non-stationarity in the relationship between

545 gauge observation and the four downscaled SPPs, which was consistent with the findings of

546 Hussain et al (2018). Therefore, as a local form of linear regression, GWRR provided an

547 effective way to fuse gauge observation with multiple SPPs.

548   [Figure 5 here]

549   Figure 6 shows the scatterplots with color density between the original satellite

550 precipitation and the estimated precipitation by GWRR model for downscaling at monthly

551 and original spatial scale (0.25°for TMPA-3B42RT, CMORPH and PERSIANN, and 0.1° for

552 GSMaP_NRT) from 2010-2017. The GWRR model for downscaling performed well for all

553 the four SPPs, with CC values ranging from 0.98 to 0.99. The model performance varied little

554 with SPP, indicating that the local regression relationship between satellite monthly

555 precipitation and monthly NDVI, elevation, slope, longitude and latitude was relative steady

556 at different resolutions (0.25° resolution and 0.1° resolution in this study), which will benefit

557 the spatial downscaling. As shown in Figure 7, the estimated precipitation by GWRR model

558 for fusion corresponded well with the rain gauge observation, with CC of 0.86. This good

559 agreement indicated that both the constructed GWRR model for downscaling and that for

560 fusion had good performance in spatial precipitation estimates.

561   [Figure 6 here]

562   [Figure 7 here]

563 ### 4.2.2 Kriging-based residual correction

564   Some researchers believe that the residuals generated by the GWR-related model have a

565 spatial correlation structure and thus can be interpolated to help explain the variation of the

566 target variable across space (Kumar et al. 2012; Harris et al. 2010; Ye et al. 2017). In our

567 merging scheme, the residuals generated by the GWRR model for downscaling and the

568   GWRR model for fusion were interpolated using ordinary Kriging and added to the model

569   estimations (termed as residual correction) to improve the prediction accuracy. To assess the

570   necessity of kriging-based residual correction, CC, ME, rBIAS and KGE for the four

571   downscaled daily SPPs and MPP before and after residual correction with reference to gauge

572   observation were calculated and compared (Table 3). For the downscaled daily SPPs, the

573   residual correction resulted in small changes in all the four indices. CC of the downscaled

574   SPP, which reflects the spatial representativeness of precipitation, increased by 0.01 for

575   TMPA-3B42RT and remained basically unchanged for CMORPH, PERSIANN,

576   GSMaP_NRT after residual correction, indicating that the residual correction contributed

577   little to the spatial downscaling step which mainly aimed to derive the spatial pattern of

578   precipitation for the fusion step. If not followed by a fusion step, residual correction isn't

579   necessary for the spatial downscaling of the four SPPs, since the KGE values kept unchanged

580   or even declined. With regard to MPP, CC and KGE increased by 0.09 (from 0.86 to 0.95)

581   and 0.18 (from 0.70 to 0.88), respectively, and ME and rBIAS decreased by half after residual

582   correction. In conclusion, kriging-based residual correction benefited the spatial

583   representativeness of all the four downscaled SPPs and both the spatial representativeness

584   and accuracy of the Merged precipitation product (MPP); thus, it was necessary for the

585   GWRR-based two-step merging scheme.

586   [Table 3 here]

587   **4.3.   Performance of the merged precipitation product**

588   **4.3.1   Merged precipitation product**

589   Figure 8 displays the precipitation maps of the original SPPs, the downscaled SPPs, the

590   gauge observation and the final merged precipitation product (MPP) on June 21, 2014. The

591   spatial pattern of the original TMPA-3B42RT was similar to the original CMORPH (except in

592   the southern region of the study area), and significantly different from the original

593   PERSIANN or GSMaP_NRT. Maintaining the consistent spatial pattern with the original

594   SPPs in overall, the downscaled ones provided more detailed information due to the

595   introduction of NDVI and topography information. The MPP, derived from gauge

596   observation and multiple downscaled SPPs, had higher accuracy and spatial

597   representativeness in contrast to any one of the downscaled SPPs.

598   [Figure 8 here]

599   Figure 9 shows the time series of gauge sites-averaged monthly accumulated

600   precipitation of gauge observation, original SPPs and MPP for the period 2010-2017. In

601   general, compared to the four original SPPs, the time series of MPP is much closer to that of

602   gauge observation, although the violent precipitation was somewhat underestimated in MPP.

603   From 2010 to 2017, the average daily precipitation of the original TMPA3B42-RT, CMORPH,

604   PERISIANN, GSMaP_NRT were 4.12 mm, 2.34 mm, 6.67 mm and 2.57 mm, respectively;

605   and that of gauge observation and MPP were 3.74 mm and 3.33 mm, respectively.

606   [Figure 9 here]

607   **4.3.2 Performance evaluation**

608   To assess the merging scheme, the continuous indices (CC, ME, rBIAS and KGE) for

609   the four original SPPs and MPP with reference to gauge observation across the entire period

610   and different seasons are listed in Table 4. All these indices of MPP got much better scores

611   than the four original SPPs, indicating that the GWRR-based two-step merging scheme

612   substantially improved the quality of the daily precipitation maps. The continuous indices of

613   MPP had best scores in winter, followed by spring, autumn and summer. Considering the

614   characteristics of the precipitation in these seasons, it can be inferred that the MPP generated

615   by the GWRR-based two-step merging scheme did not perform perfectly for light

precipitation and violent precipitation events. In addition, the performance difference among the four original SPPs shown in Table 4 revealed that each SPP had its individual strength and weakness in various seasons, which was the theoretical basis for the fusion of gauge observation and multiple SPPs.

[Table 4 here]

Taylor diagrams for daily precipitation from the gauge observation, the four original SPPs and MPP (Figure 10) were also drawn to visually compare the accuracy. In Taylor diagram, if the point of SPP is closer to the gauge point, then it is considered as a better product. Figure 10 confirms that the GWRR-based two-step merging scheme significantly improved the spatial estimates of daily precipitation.

[Figure 10 here]

Figure 11 plots the values of the four categorical indices for five classes of precipitation intensity, including no rain ([0, 1) mm/d), light rain ([1, 5) mm/d), moderate rain ([5, 20) mm/d), heavy rain ([20, 40) mm/d) and violent rain (≥ 40 mm/d). All the products, i.e., the four original SPPs and MPP, identified the no-rain events well but showed poor performance in rainy events detection. In addition, all the products overestimated the number of no-rain events and underestimated the amount of light rain, moderate rain and heavy rain event. MPP performed the best in terms of the four categorical indices for all the five rain events, with exception of the FBI for heavy rain event.

[Figure 11 here]

Figure 12 shows the KGE values for the daily precipitation of original SPPs and MPP at 42 gauge sites during 2010-2017. KGE values varied so vastly from product to product and from space to space. Among the four original SPPs, TMPA-3B42RT performed the best, with KGE values ranging from 0.48 to 0.75 at the 42 gauge sites, followed by GSMaP_NRT and CMORPH, and then the PERSIANN, with KGE values ranging from -0.57 to 0.44. There

641 was no consistent space distribution of KGE in relation to the original SPPs, for example, the

642 high KGE values for the original MPA-3B42RT, CMORPH, PERSIANN and GSMaP_NRT

643 occurred in the central, southeastern, northeastern and northwestern regions, respectively.

644 Compared with the original SPPs, MPP had much better performance in terms of KGE, with

645 values of 0.79-0.94 at the 42 gauge sites. The lowest KGE values were distributed in the

646 northwestern mountains with the highest elevation, which may be attributed to the poor

647 performance of the four original SPPs.

648   [Figure 12 here]

5. Discussion

650   The quality of MPP depends on many factors, such as the ability of SPP to capture the

651 precipitation spatial pattern, the merging algorithm and the density of rain gauge network

652 (Chao et al. 2018).

653   In terms of traditional merging algorithms, gauge observation can be merged with only

654 one SPP, and researchers need to evaluate the performance of various SPPs first to select a

655 well-performed SPP for merging, since no one SPP has proven to be superior to others for all

656 time and regions (Maggioni et al. 2016; Sun et al. 2018). Given that each SPP has its own

657 strengths and weaknesses in the capture of precipitation spatial pattern, Beck et al. (2019)

658 derived a new SPP for merging by combining lots of released SPPs together. The

659 GWRR-based merging algorithm proposed in this paper, in contrast, allows to make use of

660 the strength of each SPP, with no need for a SPP selection or multiple SPPs combination

661 process.

662   To investigate whether the introduction of multiple SPPs could improve the fusion

663 performance, we also used only one SPP to construct the GWRR model for fusion. These

664 GWRR models for fusion were constructed by replacing the independent variables of

665 Equation (21) and (22), i.e., the four Box-Cox transformed downscaled SPPs, with a single

666 transformed downscaled TMPA-3B42RT, CMORPH, PERSIANN and GSMaP_NRT, and

667 termed as $GWRR_T$, $GWRR_C$, $GWRR_P$ and $GWRR_G$, respectively. In order to avoid confusion,

668 the GWRR model for fusion with multiple Box-Cox transformed downscaled SPPs as

669 independent variables, which was expressed with Equation (21) and (22) in our two-step

670 merging scheme, was termed as $GWRR_M$ in this section.

671 Table 5 shows the evaluation statistics with reference to gauge observation for the fusion

672 models (i.e., $GWRR_T$, $GWRR_C$, $GWRR_P$, $GWRR_G$ and $GWRR_M$ model) across the entire

673 period and different seasons during 2010-2017. For the fusion of gauge observation and a

674 single SPP, $GWRR_G$ model showed the best statistical scores in the entire period, with CC of

675 0.79, ME of -1.30 mm, rBIAS of -34.9% and KGE of 0.59. By contrast, these four indices in

676 $GWRR_M$ were 0.86, -0.98 mm, -26.3% and 0.70, respectively. Furthermore, such better

677 statistical scores of $GWRR_M$ relative to $GWRR_T$, $GWRR_C$, $GWRR_P$ and $GWRR_G$ model were

678 also be found for all the seasons. Figure 13 present the KGE at 42 gauge sites for the

679 precipitation estimated by various GWRR models over the period of 2010-2017. Among the

680 GWRR models with a simple SPP as independent variable, $GWRR_G$ model had best KGE

681 scores, with values ranging from 0.46 to 0.71 at 42 gauge sites, which were inferior than that

682 for $GWRR_M$ model ranging from 0.55 to 0.82. These comparisons demonstrated that, in the

683 fusion step, the use of multiple SPPs provided more reliable spatial precipitation estimates

684 than a single SPP, which is consistent with the results obtained by Golian et al. (2015) and

685 Ma et al. (2017).

686 [Table 5 here]

687 [Figure 13 here]

688 Sparse rain gauge network density would lead to huge uncertainty, as only very few

689 samples are used for the regression coefficient calculation in GWRR and the semi-variance

690 calculation in ordinary Kriging (Jongjin et al. 2016). It is a well-known fact that the increase

691 of network density could reduce error and uncertainty in precipitation interpolation based on

692 ordinary Kriging (Adhikary et al. 2015). With regard to the merging of gauge observation and

693 SPP, increasing the gauge network density also could reduce the uncertainty and help to

694 improve the quality of MPP (Li et al. 2015; Park et al. 2017; Chen et al. 2018). However,

695 once the network density reaches a critical threshold, the quality of MPP will be not affected

696 by the increase of network density (Yang et al. 2017). The optimal network density for

697 obtaining the best-performed MPP may varies with the merging algorithms and need further

698 investigation.

6. Conclusions

700 This study proposed a two-step scheme, consisting of downscaling and fusion, for

701 merging gauge observation with multiple SPPs to improve the spatial estimates of daily

702 precipitation. Both steps of downscaling and fusion employed geographically weighted ridge

703 regression (GWRR) method, which was established by combining ridge regression with

704 GWR to overcome the potential local collinearity problem associated with GWR. Deriving

705 spatial precipitation estimates from gauge observation and four near real-time SPPs (i.e.,

706 TMPA-3B42RT, CMORPH, PERSIANN and GSMaP_NRT), with the support of NDVI and

707 DEM data, the proposed GWRR-based two-step merging scheme was applied to Xijiang

708 Basin of China from 2010 to 2017. The main findings of this study are as follows.

709 (1) Collinearity problem often occurred in the GWR model both for downscaling and for

710 fusion. The perfect collinearity problem, representing extreme cases of collinearity that

711 causes the parameter of GWR to become unsolvable, never troubled GWR model for

712 downscaling (PCR in all the regions was 0) but frequently plagued the GWR model for

713 fusion (spatially averaged PCR reached 37%).

714 (2) The relationship between gauge observation and the four downscaled SPPs (i.e.,

715 TMPA-3B42RT, CMORPH, PERSIANN and GSMaP_NRT) was spatiotemporally

716   non-stationary, and thus, GWRR, the linear regression method with time-varying and

717   space-varying regression coefficients, provided a promising method for the fusion.

718   (3) Kriging-based residual correction benefited the spatial representativeness of the

719   downscaled TMPA-3B42RT (CC increased by 0.01) and both spatial representativeness

720   (CC increased by 0.10) and accuracy (ME and rBIAS decreased by more than half, KGE

721   increased by 0.18) of the MPP; thus, it was helpful for both the GWRR-based

722   downscaling and fusion step.

723   (4) The merged precipitation product (MPP) generated by the proposed GWRR-based

724   two-step merging scheme had much higher resolution (1 km resolution) and accuracy

725   (KGE of 0.88), compared with the four original SPPs (0.25° and 0.1° resolution; KGE of

726   0.04-0.64).

727   (5) In the fusion step, the use of multiple SPPs provided more reliable spatial precipitation

728   estimates than using a single SPP. The KGE of $GWRR_M$-estimated precipitation

729   increased by 0.11 compared with that of $GWRR_G$-estimated precipitation, which

730   performed best for the fusion of gauge observation and a single SPP, with KGE of 0.59.

731   In summary, the proposed GWRR-based two-step merging scheme consisting of

732   downscaling and fusion could be successfully implemented to improve the spatial estimates

733   of daily precipitation.

Acknowledgments

References

740 Adhikary, S.K., Yilmaz, A.G., Muttil, N., 2015. Optimal design of rain gauge network in the

742 Middle Yarra River catchment, Australia. Hydrol. Processes 29, 2582-2599.

743 AghaKouchak, A., Nasrollahi, N., Habib, E., 2009. Accounting for uncertainties of the

744 TRMM satellite estimates. Remote Sens. 1, 606-619.

745 Almazroui, M., 2011. Calibration of TRMM rainfall climatology over Saudi Arabia during

746 1998-2009. Atmos. Res. 99, 400-414.

747 Baez-Villanueva, O.M., Zambrano-Bigiarini, M., Beck, H.E., McNamara, I., Ribbe, L.,

748 Nauditt, A., Birkel, C., Verbist, k., Giraldo-Osorio, J.D., Thinh, N.X., 2020, RF-MEP: A

749 novel Random Forest method for merging gridded precipitation products and ground-based

750 measurements. Remote Sens. Environ. 239, 111606.

751 Beck, H.E., van Dijk, A.I.J.M., Levizzani, V., Schellekens, J., Miralles, D.G., Martens, B., de

752 Roo, A., 2017. MSWEP: 3-hourly 0.25 degrees global gridded precipitation (1979-2015) by

753 merging gauge, satellite, and reanalysis data. Hydrol. Earth Syst. Sci. 21, 589-615.

754 Beck, H.E., Wood, E.F., Pan, M., Fisher, C.K., Miralles, D.G., Van Dijk, A.I.J.M., McVicar,

755 T.R., Adler, R.F., 2019. MSWEP V2 global 3-hourly 0.1 degrees precipitation: methodology

756 and quantitative assessment. Bull. Am. Meteorol. Soc. 473-502.

757 Belsley, D.A., Kuh, E., Welsch, R.E., 1980. Regression diagnostics: Identifying influential

758 data and sources of collinearity. New York: Wiley.

759 Bharti, V., Singh, C., 2015. Evaluation of error in TRMM 3B42V7 precipitation estimates

760 over the Himalayan region. J. Geophys. Res. Atmos. 120, 12458-12473.

761 Blu, T., Thevenaz, P., Unser, M., 2004. Linear interpolation revitalized. IEEE Trans. On

762 Image Proce. 13(5), 710-719.

763 Bowman, A.W., 1984. An alternative method of cross-validation for the smoothing of density

764 estimates. Biometrika, 71, 353-360.

765 Brunsdon, C., Charlton, M., Harris, P., 2012. Living with collinearity in local regression

766 models. In Proceedings of the 10th International Symposium on Spatial Accuracy Assessment

767 in Natural Resources and Environmental Sciences, Brasil.

768 Brunsdon, C., Fotheringham, A.S., Charlton, M., 1996. Geographically weighted regression:

769 a method for exploring spatial nonstationarity. Geogr. Anal. 28, 281-298.

770 Brunsell, N., 2006. Characterization of land-surface precipitation feedback regimes with

771 remote sensing. Remote Sens. Environ. 100, 200-211.

772 Cecinati, F., Wani, O., Rico-Ramirez, M.A., 2017. Comparing approaches to deal with

773 non-Gaussianity of rainfall data in kriging-based radar-gauge rainfall merging. Water Resour.

774 Res. 53, 8999-9018.

775 Chao, L.J., Zhang, K., Li, Z.J., Zhu, Y.L., Wang, J.F., Yu, Z.B., 2018. Geographically

776 weighted regression based methods for merging satellite and gauge precipitation. J. Hydrol.

777 558, 275-289.

778 Cheema M.J.M., Bastiaanssen, W.G.M., 2012. Local calibration of remotely sensed rainfall

779 from the TRMM satellite for different periods and spatial scales in the Indus Basin. Int. J.

780 Remote Sens. 33, 2603-2627.

781 Chen, C., Zhao, S.H., Duan, Z., Qin, Z.H., 2015. An improved spatial downscaling procedure

782 for TRMM 3B43 precipitation product using geographically weighted regression. IEEE J. Sel.

783 Top. Appl. Earth Obs. Remote Sens. 8, 4592-4604.

784 Chen, Y.Y., Huang, J.F., Sheng, S.X., Mansaray, L.R., Liu, Z.X., Wu, H.Y., Wang, X.Z., 2018.

785 A new downscaling-integration framework for high-resolution monthly precipitation

786 estimates: Combining rain gauge observations, satellite-derived precipitation data and

787 geographical ancillary data. Remote Sens. Environ. 214, 154-172.

788 Chen, F.R., Gao, Y.Q., Wang, Y.G., Qin, F., Li, X., 2019. Downscaling satellite-derived daily

789 precipitation products with an integrated framework. Int. J. Climatol. 39, 1287-1304.

790   Ciabatta, L., Massari, C., Brocca, L., Gruber, A., Reimer, C., Hahn, S., Paulik, C., Doringo,

791   W., Kidd, R., Wagner, W., 2018. SM2RAIN-CCI: a new global long-term rainfall dataset

792   derived from ESA CCI soil moisture. Earth Syst. Sci. Data 10, 267-280.

793   Delrieu, G., Wijbrans, A., Boudevillain, B., Faure, D., Bonnifait, L., Kirstetter, P.E., 2014.

794   Geostatistical radar – raingauge merging: A novel method for the quantification of rain

795   estimation accuracy. Adv. Water Resour. 71, 110-124.

796   Dinku, T., Ruiz, F. Connor, S.J., Ceccato, P., 2010. Validation and intercomparison of satellite

797   rainfall estimates over Colombia. J. Appl. Meteor. Climatol. 49, 1004-1014.

798   Duan, Z., Bastiaanssen, W.G.M., 2013. First results from Version 7 TRMM 3B43

799   precipitation product in combination with a new downscaling-calibration procedure.

800   Remote Sens. Environ. 131, 1-13.

801   Erdin, R., Frei, C., Kunsch, H.R., 2012. Data Transformation and Uncertainty in

802   Geostatistical Combination of Radar and Rain Gauges. J. Hydrometeor. 13, 1332-1346.

803   Fang, J., Du, J., Xu, W., Shi, P.J., Li, M., Ming, X.D., 2013. Spatial downscaling of TRMM

804   precipitation data based on the orographical effect and meteorological conditions in a

805   mountainous area. Adv. Water Resour. 61, 42-50.

806   Feng, S., Hu, Q., Qian, W.H., 2004. Quality control of daily meteorological data in China,

807   1951-2000: A new dataset. Int. J. Climatol. 24, 853-870.

808   Fotheringham, A.S., Brunsdon, C., Charlton, M., 2002. Geographically weighted regression:

809   the analysis of spatially varying relationships. John Wiley & Sons, Chichester, UK.

810   Gebremichael, M., Anagnostou, E.N., Bitew, M.M., 2010. Critical steps for continuing

811   advancement of satellite rainfall applications for surface hydrology in the Nile River Basin. J.

812   Amer. Water Resour. Assoc. 46, 361-366.

813   Golding, B. W., 2009. Uncertainty propagation in a London flood simulation. J. Flood Risk

814   Manage. 2, 2-15.

815   Golian, S., Moazaml, S., Kirstetter, P.E., Hong, Y., 2015. Evaluating the performance of

816   merged multi-satellite precipitation products over a complex terrain. Water Resour. Manage.

817   29, 4885-4901.

818   Gollini, I., Lu, B.B., charlton, M., Brunsdon, C., Harris, P., 2015. GW model: An R Package

819   for exploring spatial heterogeneity using geographically weighted models. J. Stat. Softw. 63,

820   1-50.

821   Gourley, J.J., Vieux, B.E., 2006. A method for identifying sources of model uncertainty in

822   rainfall-runoff simulations. J. Hydrol. 327, 68-80.

823   GPM Global Rainfall Map Algorithm Development Team, 2014. Global Satellite Mapping of

824   Precipitation (GSMaP) for GPM: Algorithm Theoretical Basis Document (Algorithm Ver.6).

825   Grimes, D.I.F., Pardo-Iguzquiza, E., Bonifacio, R., 1999. Optimal areal rainfall estimation

826   using raingauges and satellite data. J. Hydrol. 222, 9-108.

827   Gurung, P., 2017. Integration of gauge and radar rainfall to enable best simulation of

828   hydrological parameters. Hydrol. Sci. J. 62, 114-123.

829   Harris, P., Fotheringham, A.S., Crespo, R., 2010. The use of geographically weighted

830   regression for spatial prediction: an evaluation of models using simulated data sets. Math.

831   Geosci. 42, 657-680.

832   Hoerl, A.E., Kennard, R.W., 1970. Ridge regression: biased estimation for nonorthogonal

833   problems. Technometrics, 12, 55-67.

834   Hsu, K., Gao, X., Sorooshian, S., Gupta, H.V., 1997. Precipitation estimation from remotely

835   sensed information using artificial neural networks. J. Appl. Meteor. 36, 1176–1190.

836   Hsu, K., Gupta, H.V., Gao, X., Sorooshian, S., 1999. Estimation of physical variables from

837   multichannel remotely sensed imagery using a neural network: Application to rainfall

838   estimation. Water Resour. Res. 35, 1605–1618.

839   Huffman, G.J., Adler, R.F., Bolvin, D.T., Gu, G.J., Nelkin, E.J., Bowman, K.P., Hong, Y.,

840   Stocker, E.F., Wolff, D.B., 2007. The TRMM multisatellite precipitation analysis (TMPA):

841   Quasi-global, multiyear, combined-sensor precipitation estimates at fine scales. J.

842   Hydrometeor. 8, 38-55.

843   Huffman, G.J., Bolvin, D.T., Nelkin, E.J., 2017. Integrated Multi-satellitE Retrievals for GPM

844   (IMERG) Technical Documentation.

845   Huffman, G.J., Bolvin, D.T., 2018. Real-Time TRMM Multi-Satellite Precipitation Analysis

846   Data Set Documentation.

847   Hussain, Y., Satge, F., Hussain, M.B., Martinez-Carvajal, H., Bonnet, M.P., Cardenas-Soto,

848   M., Roig, H.L., Akhter, G., 2018. Performance of CMORPH, TMPA, and PERSIANN rainfall

849   datasets over plain, mountainous, and glacial regions of Pakistan. Theor. Appl. Climatol. 131,

850   1119-1132.

851   Immerzeel, W.W., Rutten, M.M., Droogers, P., 2009. Spatial downscaling of TRMM

852   precipitation using vegetative response on the Iberian Peninsula. Remote Sens. Environ. 113,

853   362-370.

854   Jia, S.F., Zhu, W.B., Lu, A.F., Yan, T.T., 2011. A statistical spatial downscaling algorithm of

855   TRMM precipitation based on NDVI and DEM in the Qaidam Basin of China. Remote Sens.

856   Environ. 115, 3069-3079.

857   Jing, W.L., Yang, Y.P., Yue, X.F., Zhao, X.D., 2016. A spatial downscaling algorithm for

858   satellite-based precipitation over the Tibetan Plateau based on NDVI, DEM, and land surface

859   temperature. Remote Sens. 8, 655.

860   Jongjin, B., Jongmin, P., Dongryeol, R., Minha, C., 2016. Geospatial blending to improve

861   spatial mapping of precipitation with high spatial resolution by merging satellite-based and

862   ground-based data. Hydrol. Processes. 30, 2789-2803.

863   Joyce, R.J., Janowiak, J.E., Arkin, P.A., Xie, P.P., 2004. CMORPH: A method that produces

864   global precipitation estimates from passive microwave and infrared data at high spatial and

865   temporal resolution. J. Hydrometeor. 5, 487-503.

866   Kling, H., Fuchs, M., Paulin, M., 2012. Runoff conditions in the upper Danube basin under

867   an ensemble of climate change scenarios. J. Hydrol. 424, 264 – 277.

868   Kumar, S., Lal, R., Liu, D.S., 2012. A geographically weighted regression kriging approach

869   for mapping soil organic carbon stock. Geoderma, 189, 627-634.

870   Lazaridis, A., 2007. A note regarding the condition number: the case of spurious and latent

871   multicollinearity. Qual. Quant. 41, 123-135.

872   Li, M. and Shao, Q.X., 2010. An improved statistical approach to merge satellite rainfall

873   estimates and raingauge data. J. Hydrol. 385, 51-64.

874   Li, H., Hong, Y., Xie, P.P., Gao, J.D., Niu, Z., Kirstetter, P., 2015. Variational merged of

875   hourly gauge-satellite precipitation in China: preliminary results. J. Geophys. Res. Atmos.

876   120 , 9897-9915.

877   Ma, Q. M., Xiong, L.J. Xia, J., Xiong, B., Yang, H., Xu, C-Y., 2019. A censored shifted

878   mixture distribution mapping method to correct the bias of daily IMERG satellite

879   precipitation Estimates. Remote Sens. 11, 1135.

880   Ma, Y.Z., Hong, Y., Chen, Y., Yang, Y., Tang, G.Q., Yao, Y.J., Long, D., Li, C.M., Han, Z.Y.,

881   Liu, R.H., 2017. Performance of optimally merged multisatellite precipitation products using

882   the dynamic Bayesian model averaging scheme over the Tibetan Plateau. J. Geophys. Res.

883   Atmos. 123, 814-834.

884   Ma, Z.Q., He, K., Tan, X., Liu, Y., Lu, H.Y., Shi, Z., 2019. A new approach for obtaining

885   precipitation estimates with a finer spatial resolution on a daily scale based on TMPA V7 data

886   over the Tibetan Plateau. Int. J. Remote Sens. 40, 8465-8583.

887   Ma, Z.Q., Shi, Z., Zhou, Y., Xu, J.F., Yu, W., Yang, Y.Y., 2017. A spatial data mining

888   algorithm for downscaling TMPA 3B43 V7 data over the Qinghai-Tibet Plateau with the

889   effects of systematic anomalies removed. Remote Sens. Environ. 200, 378-395.

890 Maggioni, V., Meyers, P.C., Robinson, M.D., 2016. A review of merged high-resolution

891 satellite precipitation product accuracy during the tropical rainfall measuring mission

892 (TRMM) era. J. Hydrometeor. 17, 1101-1117.

893 Manz, B., Buytaert, W., Zulkafli, Z., Lavado, W., Willems, B., Robles, L.A.,

894 Rodríguez-Sánchez, J.P., 2016. High-resolution satellite-gauge merged precipitation

895 climatologies of the Tropical Andes. J. Geophys. Res. Atmos. 121, 1190-1207

896 Muniz, G., Kibria, B.M.G., 2009. On some ridge regression estimators: an empirical

897 comparisons. Commun. Stat. Simul. Comput. 38, 621-630.

898 Nerini, D., Zulkafli, Z., Wang, L.P., Onof, C., Buytaert, W., Lavado-Casimiro, W., Guyot, J.L.,

899 2015. A comparative analysis of TRMM–rain gauge data merging techniques at the daily time

900 scale for distributed rainfall-runoff modeling applications. J. Hydrometeor. 16, 2153-2168.

901 Nguyen, P., Shearer, E.J., Tran, H., Ombadi, M., Hayatbini, N., Palacios, T., Huynh, P.,

902 Updegraff, G., Hsu, K., Kuligowski, B., Logan, W.S., Sorooshian, S., 2019. The CHRS Data

903 Portal, an easily accessible public repository for PERSIANN global satellite precipitation

904 data. Sci. Data, 6, 180296.

905 O'Brien, E.M., 2007. A caution regarding rules of thumb for variance inflation factors. Qual.

906 Quant. 41, 673–690.

907 Park, N.W., Kyriakidis, P., Hong, S., 2017. Geostatistical integration of coarse resolution

908 satellite precipitation products and rain gauge data to map precipitation at fine spatial

909 resolutions. Remote Sens. 9, 255.

910 Salmeron, R., Garcia, J., Garcia, C., Lopez, M.D., 2018. Transformation of variables and the

911 condition number in ridge estimation. Comput. Sta. 33, 1497-1524.

912 Shieh, G., 2011. Clarifying the role of mean centring in multicollinearity of interaction effects.

913 Br. J. Math. Stat. Psychol. 64, 462-477.

914 Sorooshian, S., AghaKouchak, A., Arkin, P., Eylander, J., Foufoula-Georgiou, E., Harmon, R.,

915 Hendrickx, J.M.H., Imam, B., Kuligowski, R., Skahill, B., Skofronick-Jackson, G., 2011.

916 Advanced concepts on remote sensing of precipitation at multiple scales. Bull. Amer. Meteor.

917 Soc. 92, 1353-1357.

918 Sun, Q.H., Miao, C.Y., Duan, Q.Y., Ashouri, H., Sorooshian, S., Hsu, K.L., 2018. A review of

919 global precipitation data sets: data sources, estimation, and intercomparisons. Rev. Geophys.

920 56, 79-107.

921 Tao, K., Barros, A.P., 2010. Using fractal downscaling of satellite precipitation products for

922 hydrometeorological applications. J. Atmos. Oceanic Technol. 27, 409-427.

923 Taylor, K. E., 2001. Summarizing multiple aspects of model performance in a single diagram.

924 J. Geophys. Res. 106, 7183–7192.

925 Ushio, T., Sasashige, K., Kubota, T., Shige, S., Okamoto, K., Aonashi, K., Inoue, T.,

926 Takahashi, N., Iguchi, T., Kachi, M., Oki, R., Morimoto, T., Kawasaki, Z.I., 2009. A kalman

927 filter approach to the Global Satellite Mapping of Precipitation (GSMaP) from combined

928 passive microwave and infrared radiometric data. J. Meteor. Soc. Japan. 87A, 137-151.

929 Verdin, A., Rajagopalan, B., Kleiber, W., Funk, C., 2015. A Bayesian kriging approach for

930 blending satellite and ground precipitation observations. Water Resour. Res. 51, 908-921.

931 Vila, D.A., de Goncalves, L.G.G., Toll, D.L., Rozante, J.R., 2009. Statistical evaluation of

932 combined daily gauge observations and rainfall satellite estimates over Continental South

933 America. J. Hydrometeor. 10, 533-543.

934 Wheeler, D., Tiefesdorf, M., 2005. Multicollinearity and correlation among local regression

935 coefficients in geographically weighted regression. J. Geogr. Sci. 7, 161-187.

936 Wheeler, D.C., 2007. Diagnostic tools and a remedial method for collinearity in

937 geographically weighted regression. Environ. Plan. A. 39, 2464-2481.

938 Xu, S.G., Wu, C.Y., Wang, L., Gonsamo, A., Shen, Y., Niu, Z., 2015. A new satellite-based

939 monthly precipitation downscaling algorithm with non-stationary relationship between

940   precipitation and land surface characteristics. Remote Sens. Environ. 162, 119-140.

941   Yang, Z.W., Hsu, K., Sorooshian, S., Xu, X.Y., Braithwaite, D., Verbist, K.M.J., 2016. Bias

942   adjustment of satellite-based precipitation estimation using gauge observations: A case study

943   in Chile. J. Geophys. Res. Atmos. 121, 3790-3806.

944   Yang, Z.W., Hsu, K., Sorooshian, S., Xu, X.Y., Braithwaite, D., Zhang, Y., Verbist, K.M.J.,

945   2017. Merging high-resolution satellite-based precipitation fields and point-scale rain gauge

946   measurements-A case study in Chile. J. Geophys. Res. Atmos. 122, 5267-5284

947   Ye, H.C., Huang, W.J., Huang, S.Y., Huang, Y.F., Zhang, S.W., Dong, Y.Y., Chen, P.F., 2017.

948   Effects of different sampling densities on geographically weighted regression kriging for

949   predicting soil organic carbon. Spat. Stat. 20, 76-91.

950   Zambrano-Bigiarini, M., Nauditt, A., Birkel, C., Verbist, K., Ribbe, L., 2017. Temporal and

951   spatial evaluation of satellite-based rainfall estimates across the complex topographical and

952   climatic gradients of Chile. Hydrol. Earth Syst. Sci. 21, 1295-1320.

953   Zhan, C.S., Han, J., Hu, S., Liu, L.M.Z., Dong, Y.X., 2018. Spatial downscaling of GPM

954   annual and monthly precipitation using regression-based algorithms in a mountainous area.

955   Adv. Meteorol. 1506017.

956   Zhang, Y.Y., Li, Y.G., Ji, X., Luo, X., Li, X., 2018. Fine-resolution precipitation mapping in a

957   mountainous watershed: geostatistical downscaling of TRMM products based on

958   environmental variables. Remote Sen. 10, 119.

959   Zhao, H.G., Yang, S.T., Wang, Z.W., Zhou, X., Luo, Y., Wu, L.N., 2015. Evaluating the

960   suitability of TRMM satellite rainfall data for hydrological simulation using a distributed

961   hydrological model in the Weihe River catchment in China. J. Geogr. Sci. 25, 177-195.

Tables

Table 1. Summary of the four near real-time SPPs used in this research

Products	Input data	Retrieval algorithm	Temporal resolution	Spatial resolution	Latency	Period	Reference
TMPA-3B42 RT	IR: GOES-IR, Meteosat-IR and MTSat-IR; PMW: TMI, SSM/I, SSMIS, AMSR-E, AMSR2, AMSU-B and MHS	Probability matching	3 hourly	0.25×0.25°	8h	2000-present	(Huffman et al. 2007; Huffman, and Bolvin, 2018)
CMORPH	IR: GOES-IR, Meteosat-IR and MTSat-IR; PMW: TMI, SSM/I, AMSR-E, and AMSU-B	Morphing technique	3 hourly	0.25×0.25°	18h	2002-present	(Joyce et al. 2004)
PERSIANN	IR: GOES-IR and Meteosat-IR; PMW: TMI, SSM/I and AMSU-B	Adaptive artificial neural network	3 hourly	0.25×0.25°	2day	2000-present	(Sorooshian et al. 2000; Nguyen et al. 2019)
GSMaP_NRT	IR: GOES-IR and Meteosat-IR; PMW: TMI, GMI, SSM/I, SSMIS, AMSR, AMSR-E, AMSR2 and AMSU-A/MHS	Kalman filter model	1 hourly	0.1×0.1°	4h	2000-present	(Ushio et al. 2009; GPM Global Rainfall Map Algorithm Development Team 2014)

Note: IR: infrared radiance; PMW: polar-orbiting microwave; MTSAT-IR: infrared sensors on Multifunctional Transport Satellite (MTSat); Meteosat-IR: infrared sensors on Meteosat; Geo-IR: infrared sensors on geostationary (GEO) satellites; TMI: TRMM Microwave Imager; GMI: GPM Microwave Imager; SSM/I: the Special Sensor Microwave Imager on the Defense Meteorological Satellite Program (DMSP) satellites; SSMIS: the Special Sensor Microwave Imager/Souder (SSMIS) on the DMSP satellites; AMSR: Advanced Microwave Scanning Radiometer on the ADEOS-II satellites; AMSR-E: Advanced Microwave Scanning Radiometer-Earth Observing Systems on the Aqua satellites; AMSR2: Advanced Microwave Scanning Radiometer on the Global Change Observing Mission-Water (GCOM-W1) satellites; AMSU-A: Advanced

Microwave Sounding Unit-A on the NOAA-series and MetOp satellites; AMSU-B: Advanced Microwave Sounding Unit-B on the NOAA-series satellites; MHS: Microwave Humidity Sounder (MHS) on later NOAA-series satellites and the European Operational Meteorological satellite.

Table 2. List of the statistical metrics used in the performance evaluation.

Statistical Indices	Equation	Comments	Optimum score
Correlation coefficient (CC)	$CC = \dfrac{\sum_{i=1}^{n}(S_i - \bar{S})(O_i - \bar{O})}{\sqrt{\sum_{i=1}^{n}(S_i - \bar{S})^2} \times \sqrt{\sum_{i=1}^{n}(O_i - \bar{O})^2}}$	n, the number of samples; S_i, the estimated precipitation; O_i, the observed precipitation;	1
Mean error (ME)	$ME = \dfrac{1}{n}\sum_{i=1}^{n}(S_i - O_i)$	$\bar{S}$, the mean of estimated precipitation; $\bar{O}$, the mean of observed precipitation. σ_s, the standard deviations of estimated precipitation	0
Relative bias (rBIAS)	$rBIAS = \dfrac{\sum_{i=1}^{n}(S_i - O_i)}{\sum_{i=1}^{n}O_i} \times 100\%$	σ_o, the standard deviations of observed precipitation	0%
Modified Kling-Gupta efficiency (KGE)	$KGE = 1 - \sqrt{(CC-1)^2 + \left(\dfrac{\bar{S}}{\bar{O}}\right)^2 + \left(\dfrac{\sigma_s/\bar{S}}{\sigma_o/\bar{O}} - 1\right)^2}$		1
Centered root mean square difference (RMSD)	$RMSD = \sqrt{\dfrac{1}{n}\sum_{i=1}^{n}\left[(O_i - \bar{O}) - (S_i - \bar{S})\right]^2}$		0
Probability of detection (POD)	$POD = \dfrac{H}{H + M}$	H, the precipitation events reported correctly by gauge and satellite-based products; F, the precipitation events detected by satellite products but not recorded by the gauge; M, the precipitation events recorded by gauge but not detected by satellite products.	1

False alarm ratio (FAR)	$FAR = \dfrac{F}{H+F}$	0
Frequency bias index (FBI)	$FBI = \dfrac{H+F}{H+M}$	1
Critical success index (CSI)	$CSI = \dfrac{H}{H+M+F}$	1

Table 3. Evaluation statistics for the downscaled satellite precipitation and fused precipitation before and after kriging-based residual correction with reference to gauge observation during 2010-2017.

Indices		Downscaling				Fusion
		TMPA-3B42RT	CMORPH	PERSIANN	GSMaP_NRT	
CC	before residual correction	0.60	0.57	0.47	0.59	0.86
	after residual correction	0.61	0.57	0.47	0.59	0.95
ME (mm)	before residual correction	0.38	-1.49	4.81	-1.22	-0.98
	after residual correction	0.39	-1.47	4.91	-1.22	-0.41
RMSE (mm)	before residual correction	12.26	10.09	33.91	9.53	5.96
	after residual correction	12.29	10.15	34.57	9.63	3.51
rBIAS (%)	before residual correction	10.3	-39.9	128.9	-32.7	-26.3
	after residual correction	10.6	-39.6	131.8	-32.7	-10.9
KGE	before residual correction	0.54	0.25	-0.46	0.44	0.70
	after residual correction	0.54	0.25	-0.48	0.44	0.88

Table 4. Evaluation statistics for the four original SPPs and the MPP with reference to gauge observation across the entire period and different seasons during 2010-2017.

	Indices	TMPA-3B32RT	CMORPH	PERSIANN	GSMaP_NRT	MPP
Entire period	CC	0.67	0.61	0.52	0.59	0.95
	ME (mm)	0.45	-1.40	2.92	-1.17	-0.41
	rBIAS (%)	12.0	-37.6	78.4	-31.5	-10.9
	KGE	0.64	0.35	0.04	0.43	0.88
Spring	CC	0.67	0.64	0.54	0.54	0.96
	ME (mm)	0.67	-0.92	3.21	-1.35	-0.35
	rBIAS (%)	18.2	-24.7	86.5	-36.4	-9.4
	KGE	0.61	0.50	0.01	0.33	0.90
Summer	CC	0.65	0.59	0.51	0.59	0.94
	ME (mm)	1.49	-1.97	9.37	-1.37	-0.89
	rBIAS (%)	21.3	-28.1	133.9	-19.5	-12.8
	KGE	0.59	0.43	-0.42	0.53	0.86
Autumn	CC	0.69	0.63	0.46	0.63	0.96
	ME (mm)	-0.44	-1.84	-0.36	-1.51	-0.29
	rBIAS (%)	-14.3	-60.4	-11.6	-49.5	-9.7
	KGE	0.64	0.16	0.10	0.32	0.89
Winter	CC	0.67	0.64	0.39	0.57	0.99
	ME (mm)	0.08	-0.89	-0.44	-0.46	-0.10
	rBIAS (%)	7.0	-74.5	-37.3	-38.7	-8.3
	KGE	0.27	-0.21	-0.44	0.06	0.91

Table 5. Evaluation statistics with reference to gauge observation for various fusion models (i.e., $GWRR_T$, $GWRR_C$, $GWRR_P$, $GWRR_G$ and $GWRR_M$ model) across the entire period and different seasons during 2010-2017.

	Indices	$GWRR_T$	$GWRR_C$	$GWRR_P$	$GWRR_G$	$GWRR_M$
Entire period	CC	0.78	0.78	0.75	0.79	0.86
	ME(mm)	-1.41	-1.43	-1.58	-1.30	-0.98
	rBIAS(%)	-37.7	-38.3	-42.5	-34.9	-26.3
	KGE	0.56	0.55	0.51	0.59	0.70
Spring	CC	0.79	0.81	0.76	0.79	0.87
	ME(mm)	-1.32	-1.28	-1.48	-1.30	-0.91
	rBIAS(%)	-35.6	-34.5	-40.0	-35.1	-24.5
	KGE	0.59	0.60	0.54	0.59	0.72
Summer	CC	0.74	0.74	0.71	0.75	0.84
	ME(mm)	-2.78	-2.86	-3.08	-2.58	-1.94
	rBIAS(%)	-39.6	-40.8	-44.0	-36.9	-27.7
	KGE	0.53	0.51	0.47	0.56	0.68
Autumn	CC	0.81	0.79	0.78	0.82	0.88
	ME(mm)	-1.14	-1.21	-1.31	-0.99	-0.78
	rBIAS(%)	-37.3	-39.6	-43.1	-32.5	-27.0
	KGE	0.57	0.55	0.50	0.63	0.72
Winter	CC	0.88	0.90	0.86	0.90	0.93
	ME(mm)	-0.41	-0.38	-0.47	-0.35	-0.31
	rBIAS(%)	-34.3	-32.2	-39.7	-29.5	-26.2
	KGE	0.60	0.62	0.56	0.66	0.69

Figures
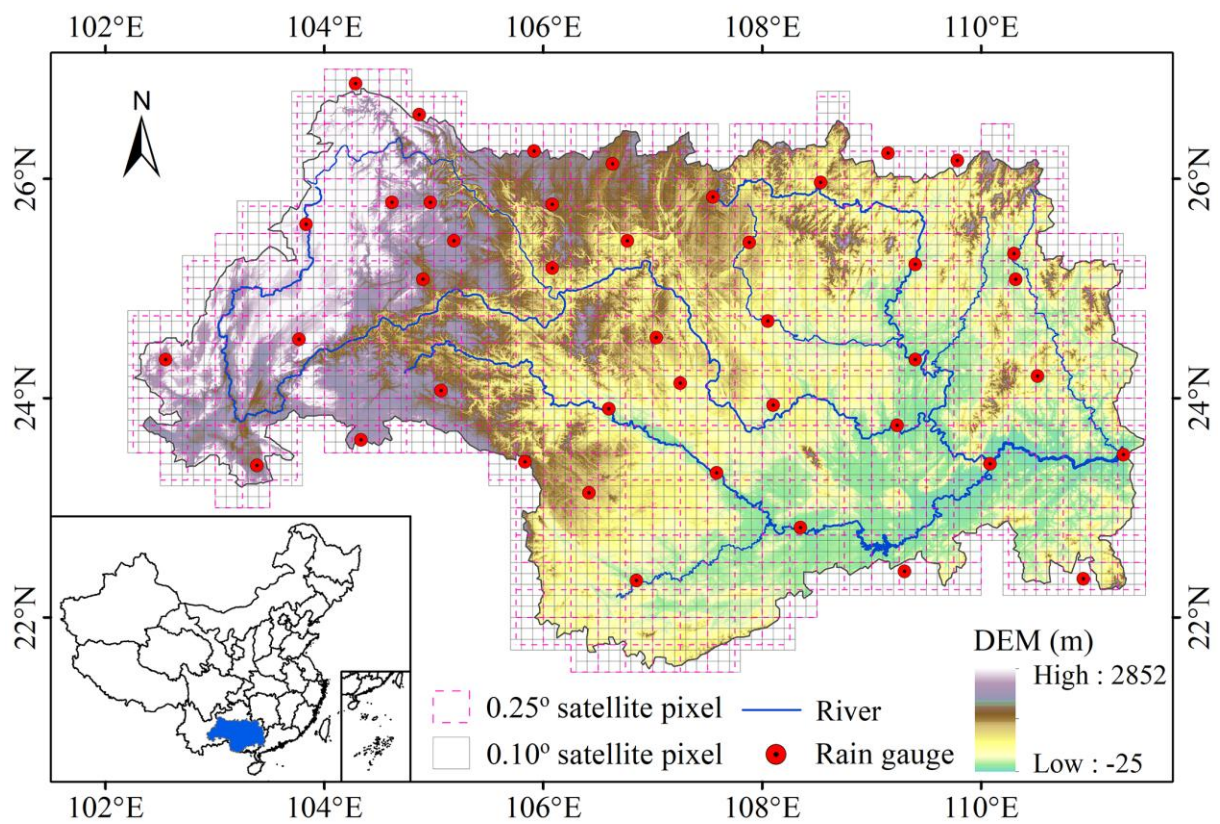
Figure 1. Location of the study area, distributions of 42 gauge sites and satellite pixels used in this study
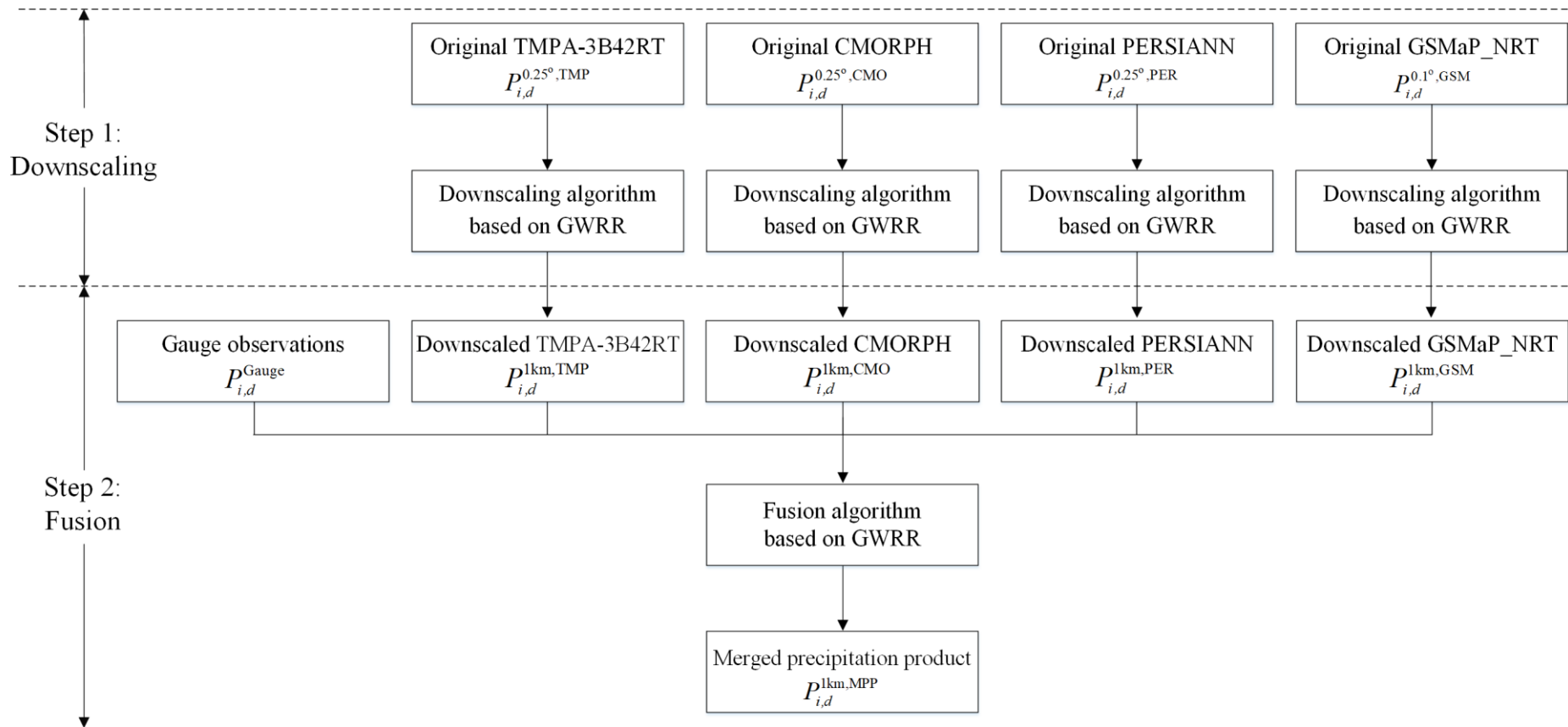
Figure 2. Flowchart of the GWRR-based two-step merging scheme proposed in this study. Noting that the subscript i and d refer to the sequence number of location and day, respectively.
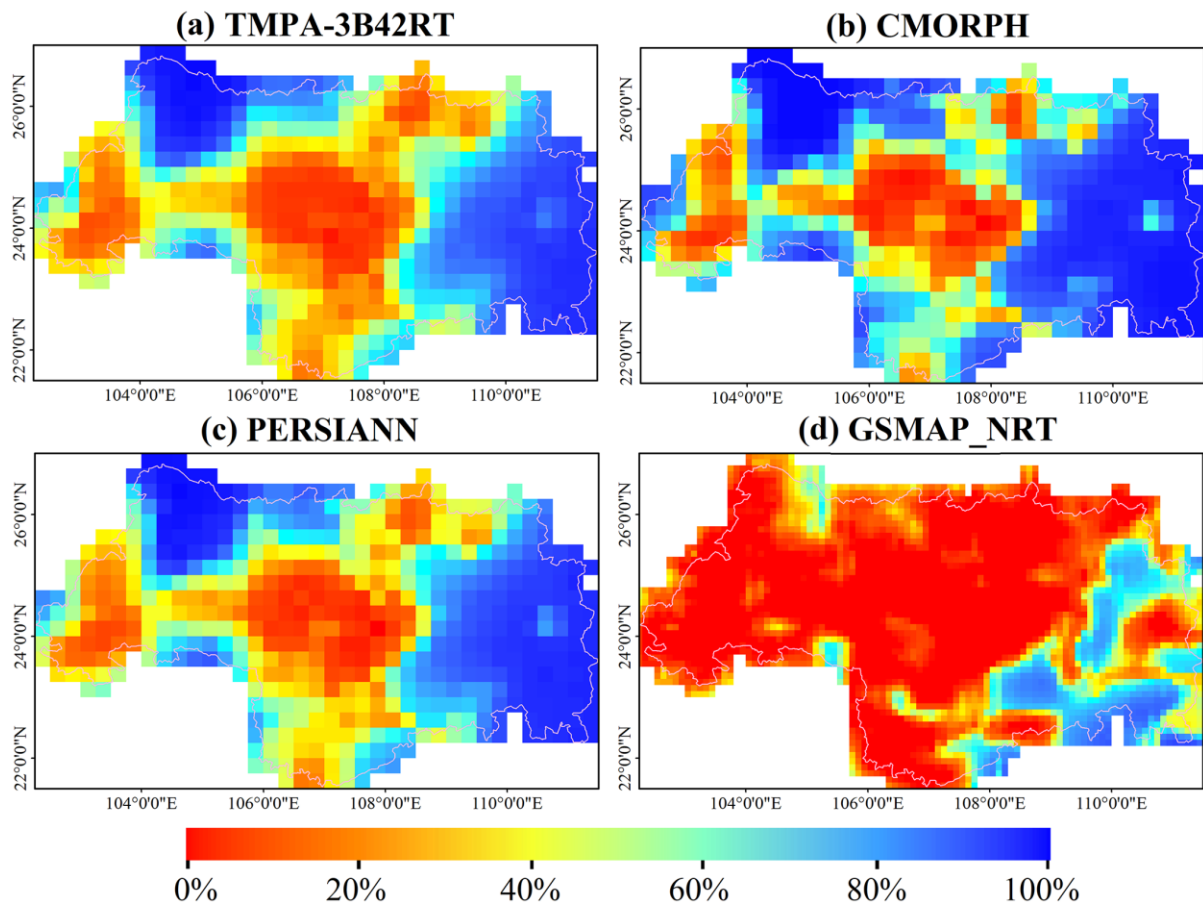
Figure 3. Spatial patterns of the collinearity rate (CR) in the GWR model for downscaling developed for (a) TMPA-3B42RT, (b) CMORPH, (c) PERSIANN, and (d) GSMaP_NRT during 2010-2017.
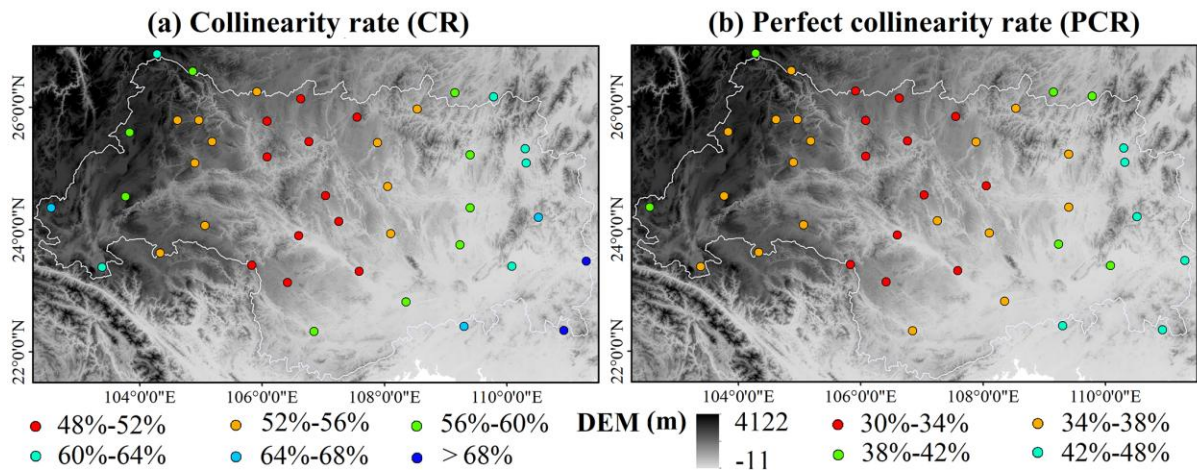
Figure 4. Spatial distributions of the (a) collinearity rate (CR) and (b) perfect collinearity rate (PCR) in the GWR model for fusion at 42 gauge sites during 2010-2017.
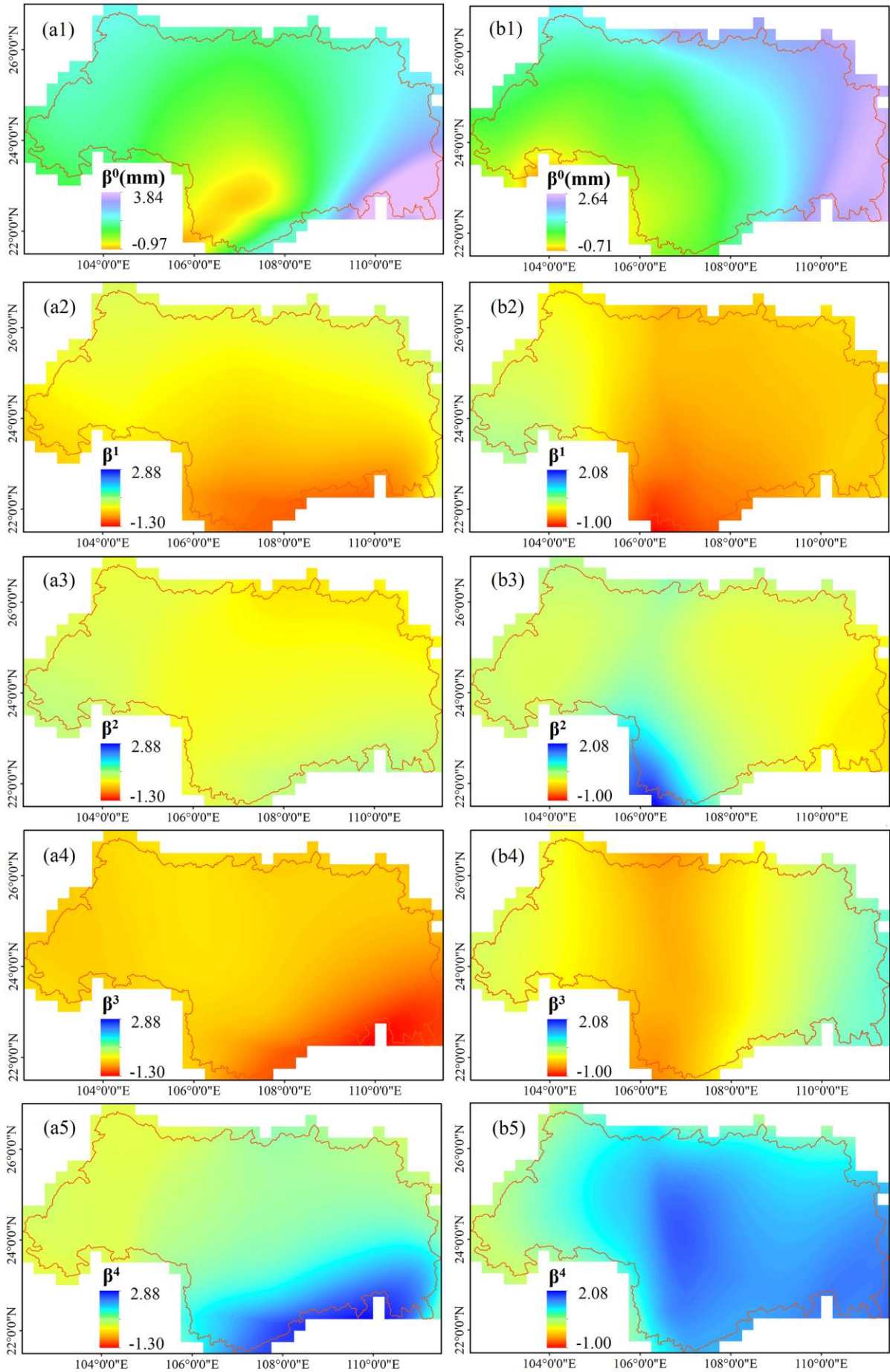
Figure 5 Spatial patterns of regression coefficients generated by the GWRR model for fusion on (left) June 21, 2014 and (right) September 30, 2014. Label (1) is the intercept, and labels (2)-(5) are the slopes of the Box-Cox transformed downscaled TMPA-3B42RT, CMORPH, PERSIANN and GSMaP_NRT precipitation. Noting that only the values with light orange are close to zero.
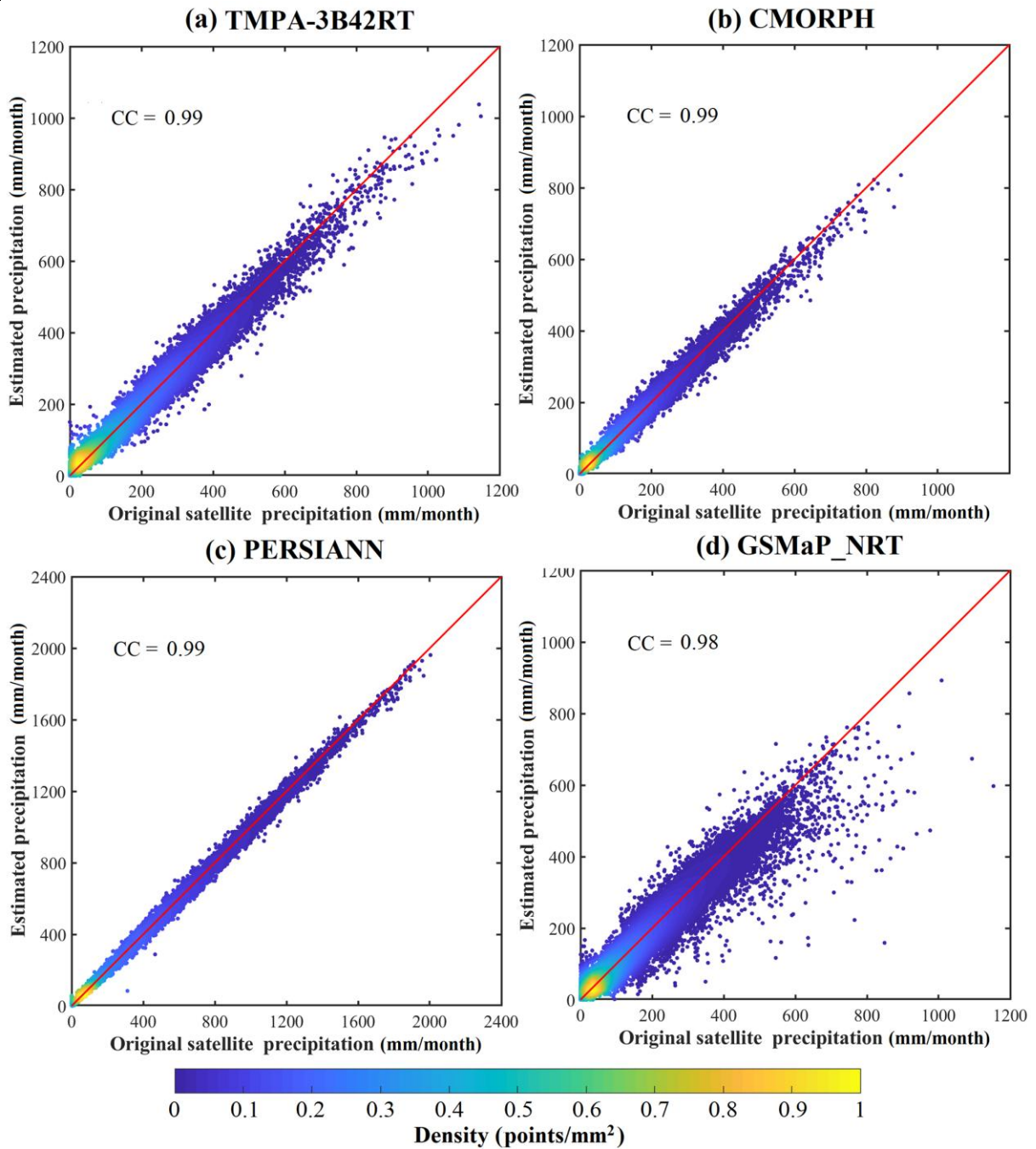
Figure 6. Scatter plots with color density between the original satellite precipitation and the estimated precipitation by the GWRR model for downscaling at monthly and original spatial scale for (a) TMPA-3B42RT, (b) CMORPH, (c) PERSIANN and (d) GSMaP_NRT from 2010-2017.
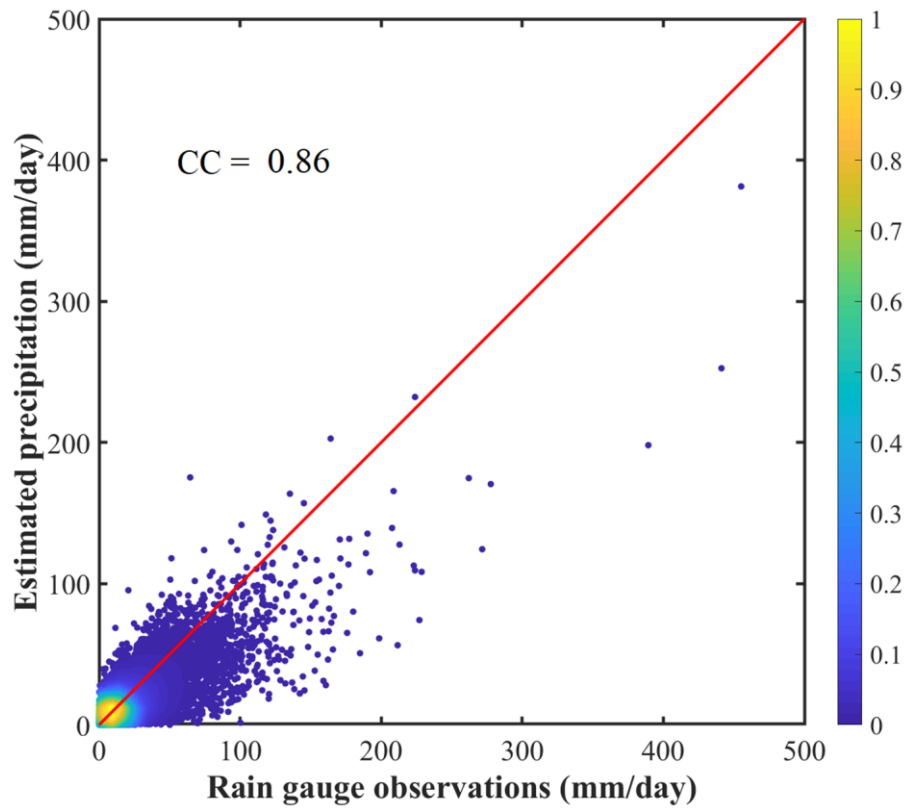
Figure 7. Scatter plots with color density between rain gauge observation and the estimated precipitation by the GWRR model for fusion from 2010-2017.
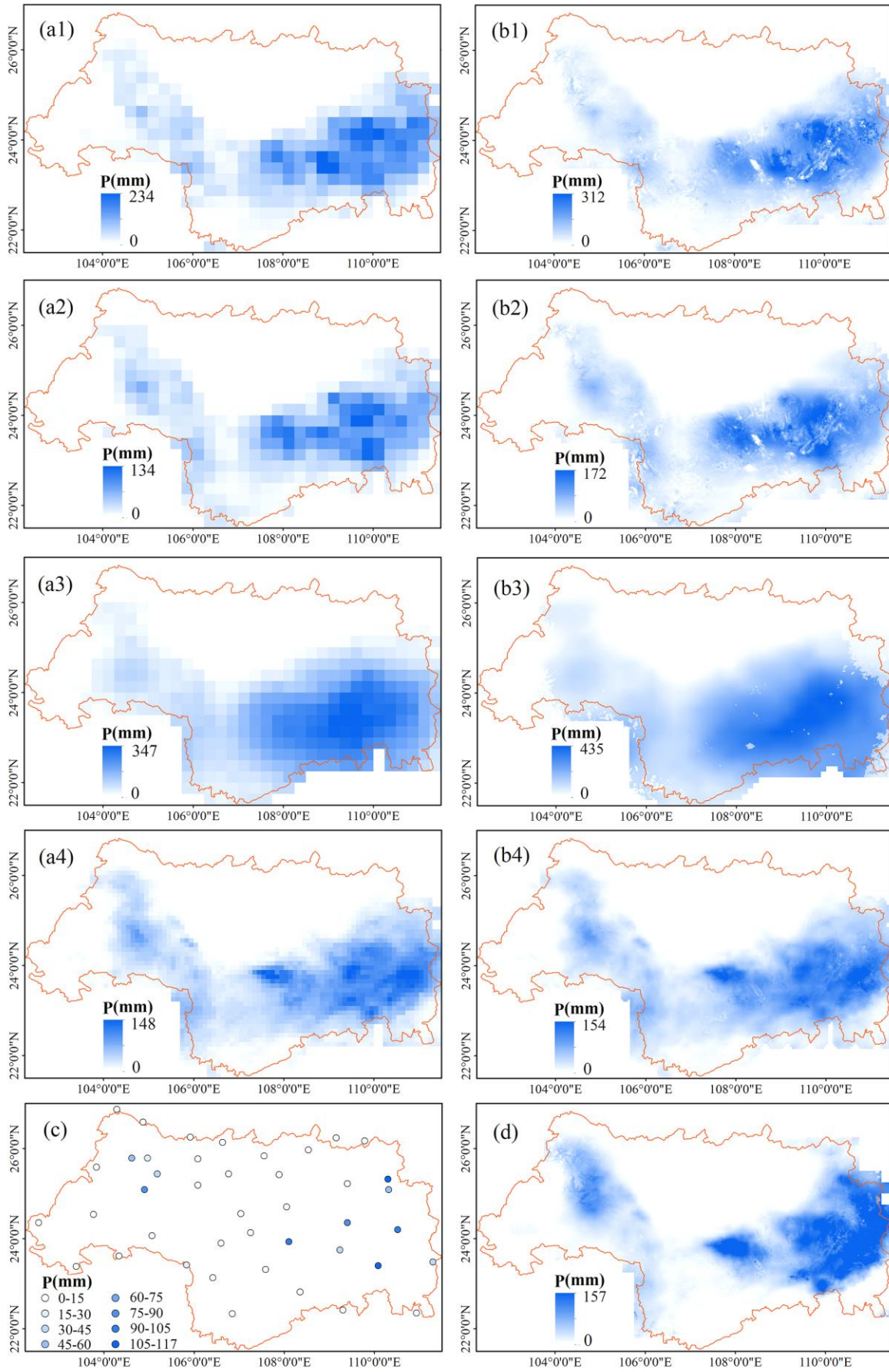
Figure 8. Precipitation maps of (a1) the original 3B42RT with 0.25° resolution; (a2) the original CMORPH with 0.25° resolution; (a3) the original PERSIANN with 0.25° resolution; (a4) the original GSMaP_NRT with 0.1° resolution; (b1) the downscaled 3B42RT with 1km resolution; (b2) the downscaled CMORPH with 1km resolution; (b3) the downscaled PERSIANN with 1km resolution; (b4) the downscaled GSMaP_NRT with 1km resolution; (c) the gauge observation; and (d) the merged precipitation product (MPP) with 1km resolution on June 21, 2014.

962
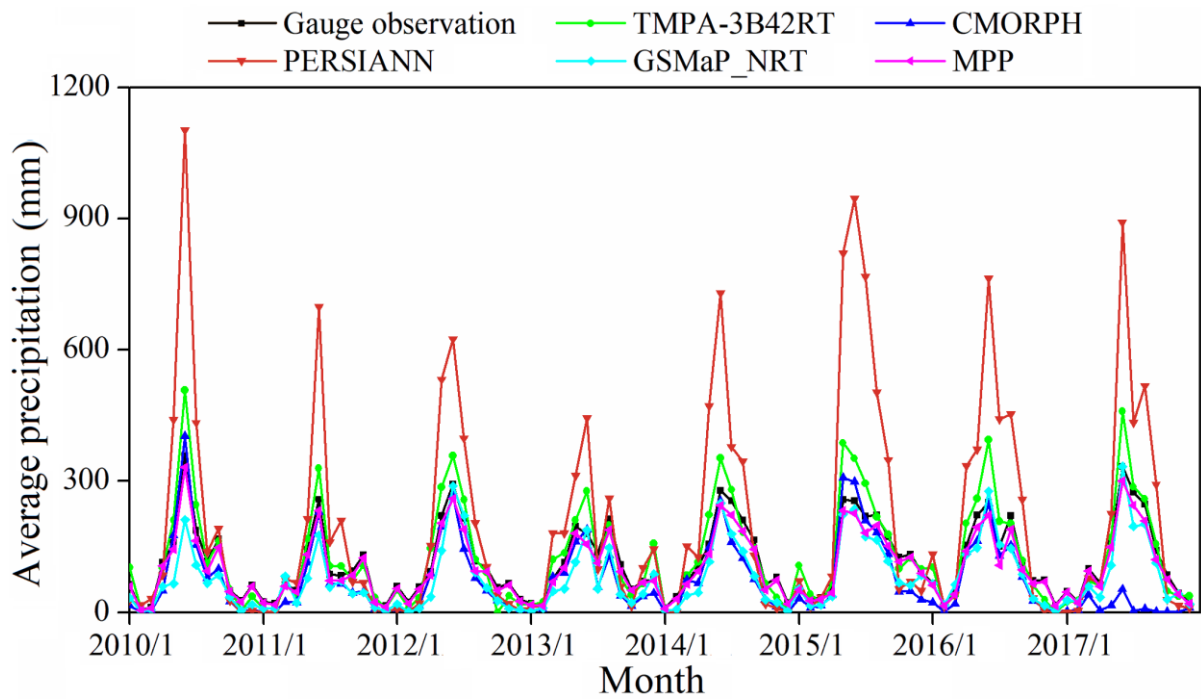
Figure 9. Time series of areal-average monthly precipitation of gauge observation, original SPPs (i.e., TMPA-3B42RT, CMORPH, PERSIANN and GSMaP_NRT) and MPP for the period 2010-2017
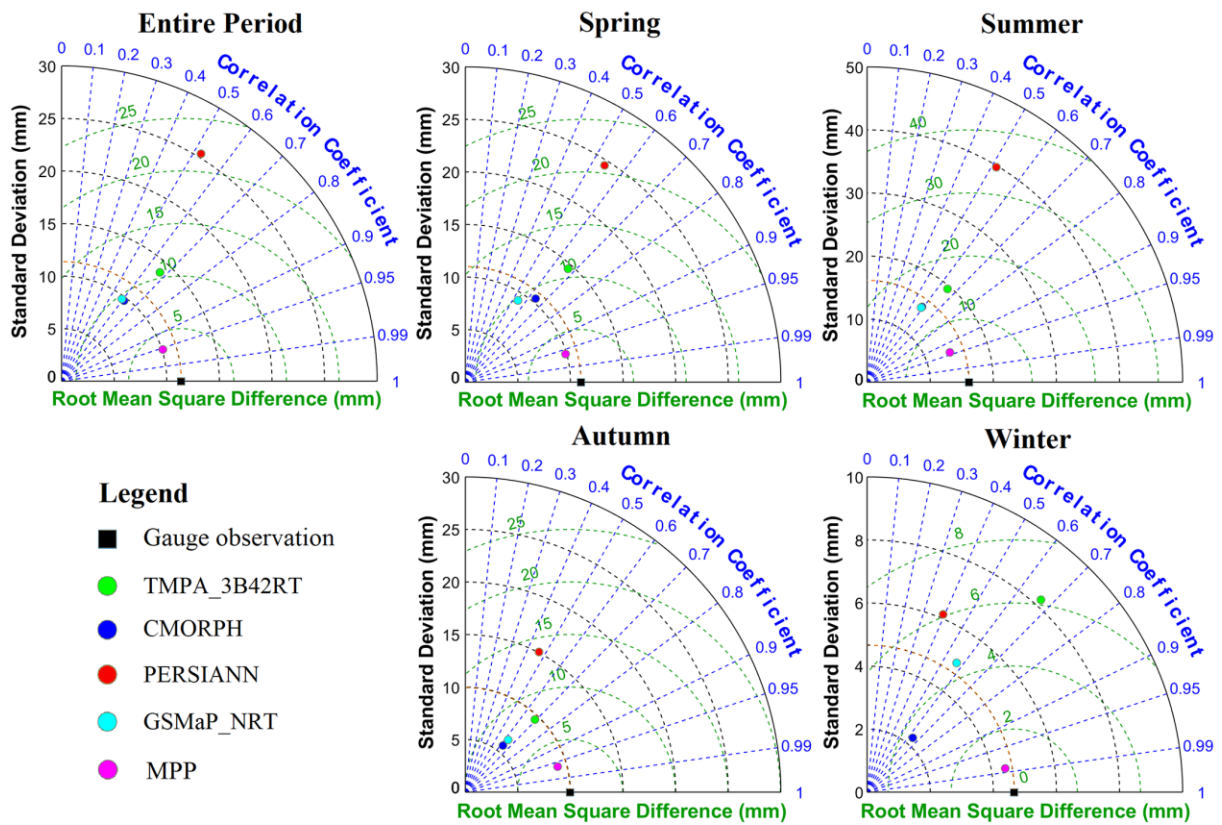
Figure 10. Taylor diagrams for daily precipitation of gauge observation, original SPPs (i.e., TMPA-3B42RT, CMORPH, PERSIANN and GSMaP_NRT) and MPP across the entire period and different seasons during 2010 to 2017.
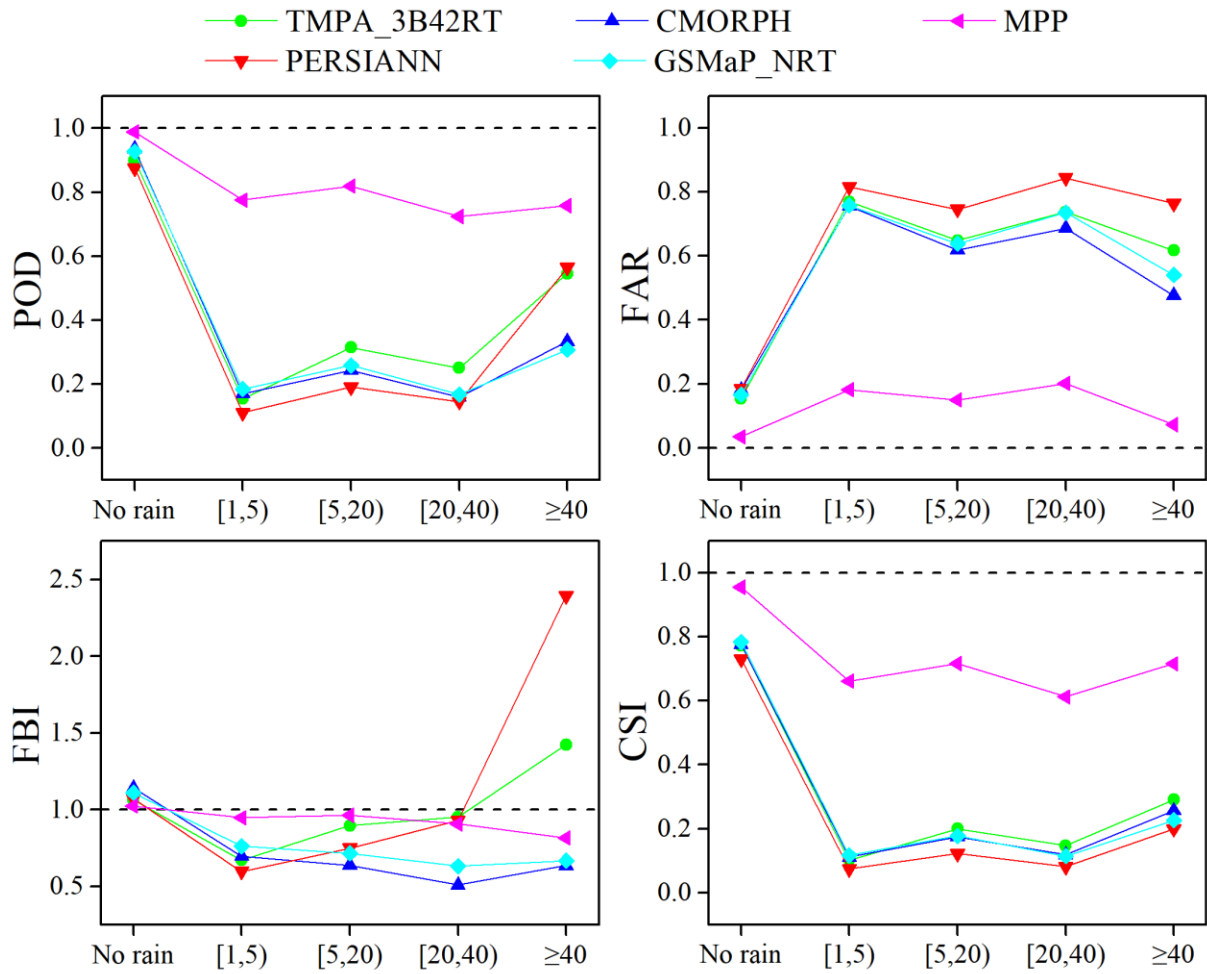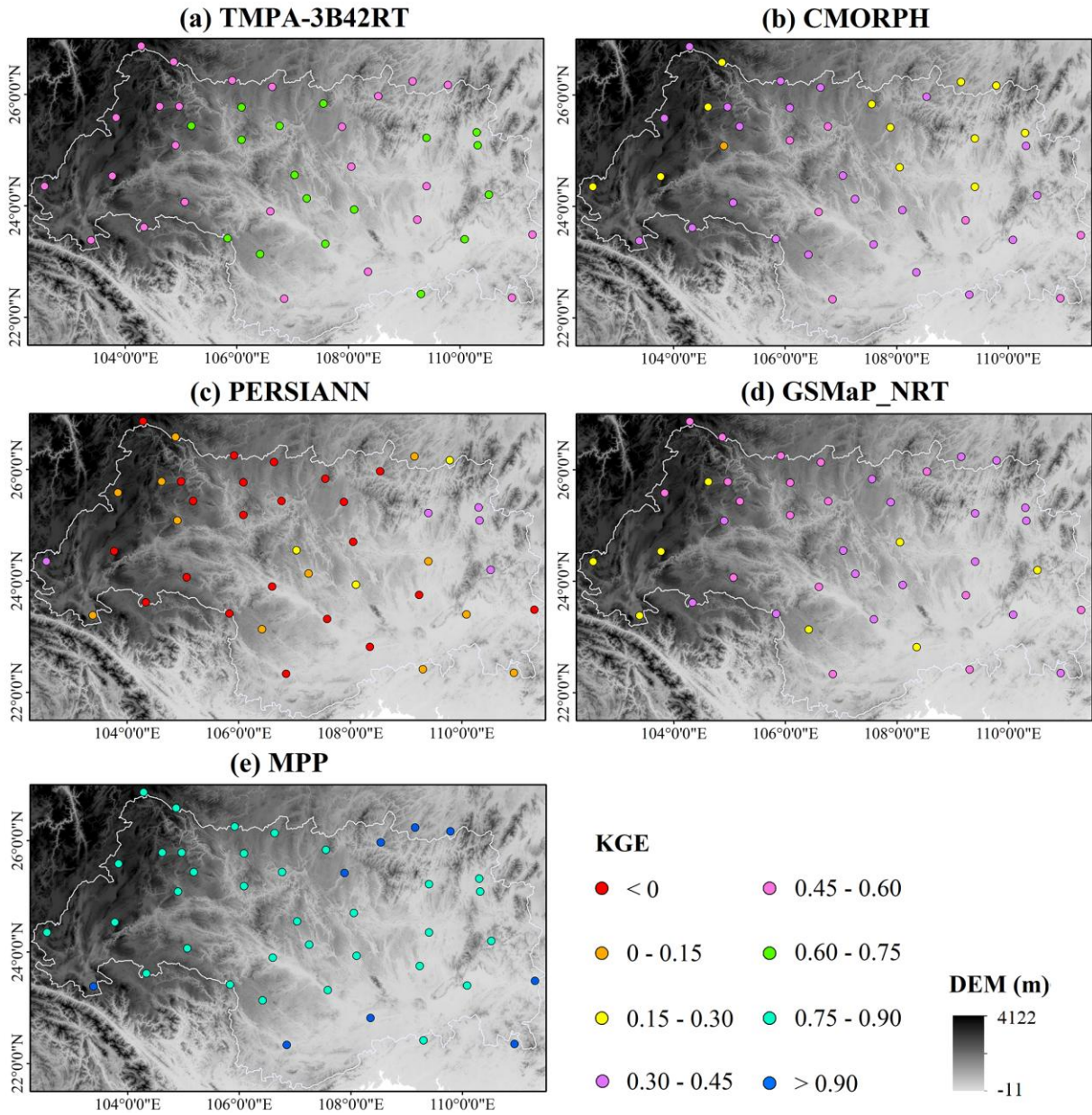
Figure 11. Evaluation statistics for categorical indices at five precipitation intensity classes (in mm/d). From left to right and top to bottom: POD, FAR, FBI and CSI. The black line represents the optimal value of each index.
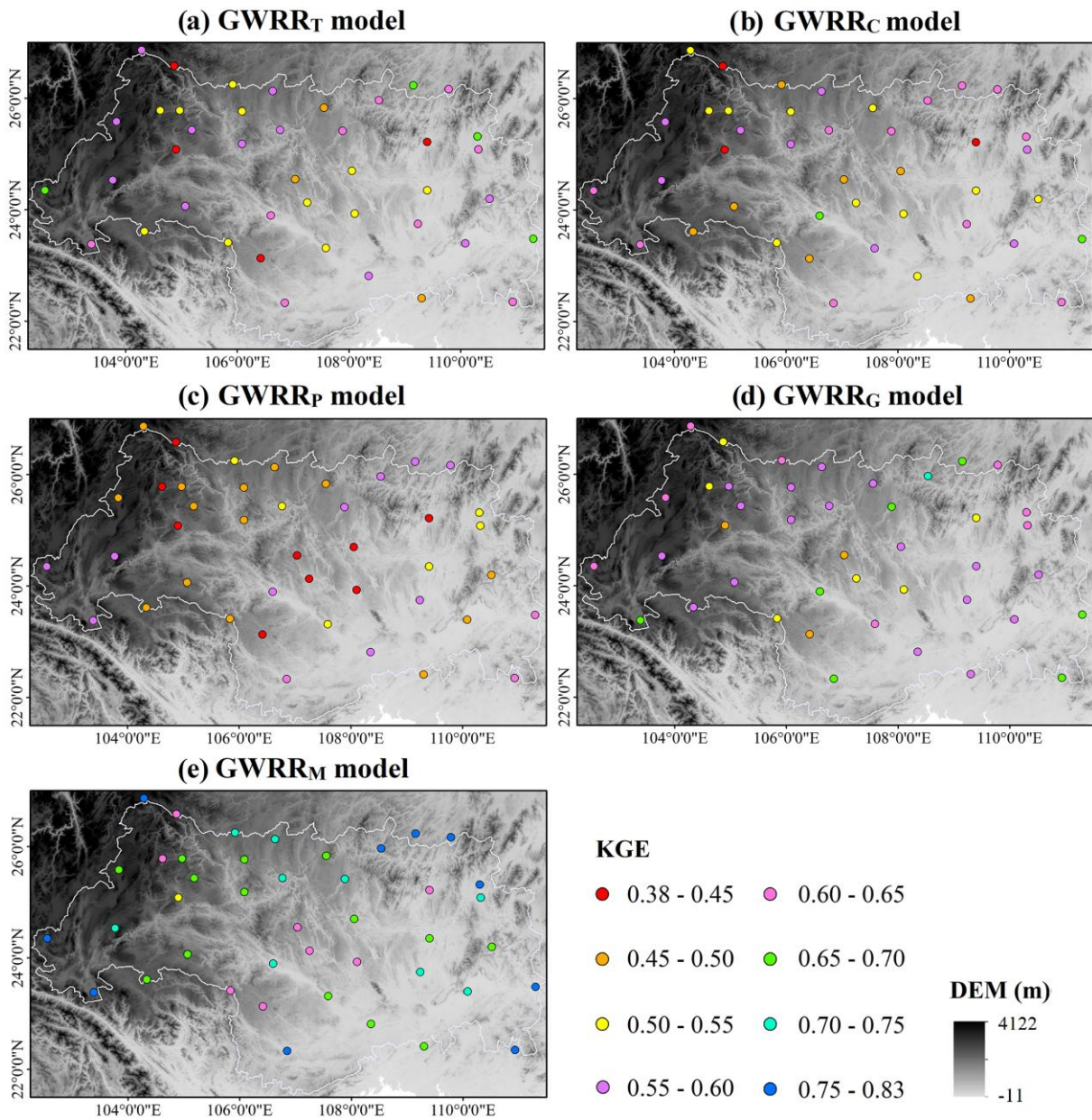
Figure 12. Modified Kling-Gupta efficiency (KGE) for daily precipitation of original SPPs (i.e., TMPA-3B42RT, CMORPH, PERSIANN and GSMaP_NRT) and MPP based on Equation (23) at 42 gauge sites during 2010-2017.

968

Figure 13. Modified Kling-Gupta efficiency (KGE) for daily precipitation estimated by (a) $GWRR_T$ model, (b) $GWRR_C$ model, (c) $GWRR_P$ model, (d) $GWRR_G$ model and (e) $GWRR_M$ model at 42 gauge sites during 2010-2017.